

# Optomechanical Crystal Devices

Amir H. Safavi-Naeini and Oskar Painter

**Abstract** We present the basic ideas and techniques utilized in recent work on optomechanical crystals. Optomechanical crystals are nanofabricated cavity optomechanical systems where the confinement of light and motion is obtained by nanopatterning periodic structures in thin-films. In this chapter we start from a basic review of the properties of optical and elastic waves in nanostructures, before introducing the properties and design of periodic structures. After reviewing fabrication and characterization methods, experimental results in 1D and 2D systems are presented.

## 1 Introduction

Nanofabricated devices and systems comprise a major recent strand of research in the field of cavity optomechanics. The first motivation pushing these developments is the promise of lower mass resonators with significantly larger optical and mechanical field localization. These structures would in principle offer larger optomechanical coupling strengths than would be typically possible in a Fabry-Pérot geometry. A second motivation arises from opportunities in development of more complex optomechanical systems with many elements. In addition to basic linear information conversion [1] and storage [2], these systems would allow observation of nontrivial collective dynamics [3, 4], as well as realization of novel many-body interactions involving spatially separated phonons and photons [5]. To control and engineer phonons, photons, and their interactions in a scalable manner, develop-

---

Amir H. Safavi-Naeini  
California Institute of Technology (Pasadena), currently at ETH Zürich and Stanford University,  
e-mail: safavi@stanford.edu

Oskar Painter  
California Institute of Technology (Pasadena) and the Max Planck Institute for the Science of Light  
(MPL), e-mail: opainter@caltech.edu

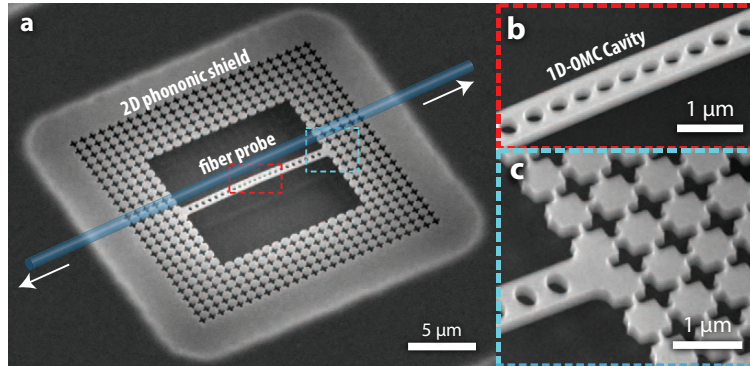


**Fig. 1 a**, A scanning electron microscope (SEM) image of an optomechanical crystal cavity formed from the top Si layer of a silicon-on-insulator chip. The device consists of **b**, a 1D-OMC cavity embedded in **c**, a phononic crystal shield. Coupling to the 1D-OMC cavity is achieved by bringing a fiber taper probe (illustrated in **a**) into the near field of the optical cavity.

ment of easily realizable structures providing control over localized excitations on the surface of a chip is required.

In this chapter one approach to the development of such structures – called “optomechanical crystals” (OMCs) is outlined. A typical optomechanical crystal system used in several recent experiments [6, 7, 8, 9, 10] is shown in Fig. 1. A pattern has been etched into a thin-film of silicon (Si) with the spacing and shape of the holes designed to give rise to localized optical and mechanical resonances in the center of the 1D-OMC beam. We will show in this chapter that the interaction between these resonances is described well by the optomechanical Hamiltonian. To understand the operation of these devices, we introduce the theoretical and experimental framework required to design, fabricate, and characterize OMC systems. This chapter is intended to give the reader an understanding of the function and design of every element of the OMC device shown in Fig. 1. Our main goal is to outline the device physics, and thus details of the experiments and potential applications of optomechanical crystals are not presented. For a thorough investigation of these details and the effects of quantum and classical noise in OMC experiments, we refer the reader to Ref. [11].

We start in this section by reviewing the quantized theory of photons and phonons in structures. In Section 2.1-2.2 the role of periodicity and symmetry in engineering the spectrum and interactions of light and sound in a solid-state setting are studied. In Section 2.3 we see that by engineering local modifications in such substrates, optical and mechanical excitations can be localized in 0- and 1-dimensional defects, *i.e.* optomechanical crystal cavities and waveguides. Recipes and formulas for calculating the couplings between phonons and photons are presented in Section 2.4. The experimental demonstrations of these ideas are reviewed in Section 3, where after a brief review of fabrication and optical probing techniques, we turn our focus onto “nanobeam” (1D-OMC) and “snowflake” (2D-OMC) structures in Section 3.3.

Finally, in Section 4, we conclude this chapter by presenting future developments that are expected to allow these engineered structures to realize their full potential.

First we begin with a review of the classical field theory of light and motion in a solid. The artificially patterned nanostructures studied in this chapter do not permit exact closed-form solutions for the electromagnetic and displacement fields and their resonant frequencies. Instead, computational software packages such as COMSOL [12] and MPB [13], developed to understand the *classical* electromagnetics and elastodynamics of solids, are used. The quantization of these fields, which is treated below, allows us to make a link between the computational methods developed over decades for classical engineering applications, and the quantum optomechanical Hamiltonian.

### ***1.1 Maxwell's equations for a photonic resonator and second quantization***

Optically, we describe the nanofabricated structure with an inhomogeneous dielectric tensor  $\bar{\bar{\epsilon}}(\mathbf{r})$ . In most of this work,  $\bar{\bar{\epsilon}}(\mathbf{r}) = \epsilon_{\text{Si}}$  in regions containing Si, and  $\bar{\bar{\epsilon}}(\mathbf{r}) = \epsilon_0$  otherwise. The time-harmonic Maxwell's equations for such a system are given by:

$$\text{curl } \mathbf{E}(\mathbf{r}) = i\omega\mu_0\mathbf{H}(\mathbf{r}), \quad \text{curl } \mathbf{H}(\mathbf{r}) = -i\omega\bar{\bar{\epsilon}}(\mathbf{r}) \cdot \mathbf{E}(\mathbf{r}). \quad (1)$$

In the absence of a source, these equations lead to self-sustaining fields, or modes, represented by transverse (or solenoidal) and longitudinal (irrotational) eigenvectors, with the eigenvalue problem for the transverse magnetic fields given by

$$\mathbf{L}\mathbf{h}_j = \omega_j^2\mathbf{h}_j, \quad \mathbf{L}(\cdot) = c^2 \text{curl} \left[ \frac{\epsilon_0}{\bar{\bar{\epsilon}}(\mathbf{r})} \text{curl} (\cdot) \right]. \quad (2)$$

Additionally, for completeness, the irrotational fields given by  $\mathbf{g}_j = \text{grad } \psi_j$ , satisfying appropriate boundary conditions, where  $\psi_m$  is an eigenvector of  $\text{div grad } \psi_j = -v_j\psi_j$  must also be considered [14], though these solutions don't play a role in the optical response of the system. This normal mode prescription is always valid for a volume enclosed inside a perfectly reflective boundary. In the limit of an open system, such as the dielectric cavities presented here, complications arise since the resonances are typically not normal modes, but so-called 'quasi-normal' resonances. We use a finite-element-method (FEM) software package, COMSOL [12] to solve eqn. (2) with open or 'scattering' boundary conditions enclosing the simulation space. The very small loss rates for the obtained resonances, informs us of the validity of the normal-mode approximation which is used throughout this work. As such, we take the numerically calculated high- $Q$  solutions with frequency  $\omega_j$  and field profile  $\mathbf{h}_j(\mathbf{r})$  to be normal modes of the structures, and then add in losses

‘by hand’ (by assuming linear coupling to a bath of linear oscillators) to take into account the effects of a finite  $Q$ .

Quantization of the transverse electromagnetic field is accomplished in the standard way (see for example Ref. [15]) by associating bosonic creation and annihilation operators,  $\hat{a}_j^\dagger$  and  $\hat{a}_j$  respectively, with each modal solution  $\{\mathbf{h}_j(\mathbf{r}), \mathbf{e}_j(\mathbf{r})\}$  of Maxwell’s equation. The field operators are expressed in the Heisenberg picture as

$$\hat{\mathbf{H}}(\mathbf{r}) = \sum_j \mathbf{h}_j(\mathbf{r}) \hat{a}_j e^{-i\omega_j t} + \text{h.c.}, \quad (3)$$

$$\hat{\mathbf{E}}(\mathbf{r}) = \sum_j \mathbf{e}_j(\mathbf{r}) \hat{a}_j e^{-i\omega_j t} + \text{h.c.}, \quad (4)$$

and we obtain from eqn. (1) that  $\mathbf{e}_j(\mathbf{r}) = i\omega_j^{-1} \overline{\overline{\boldsymbol{\epsilon}^{-1}}}(\mathbf{r}) \cdot \text{curl } \mathbf{h}_j(\mathbf{r})$ . To calculate the proper normalization of the field profiles, we assume a single photon state  $|\psi\rangle = |1\rangle_j \prod_{\forall k \neq j} |0\rangle_k$  and find the expected value of additional field energy above vacuum ( $|\text{vac}\rangle = \prod_k |0\rangle_k$ ):

$$\begin{aligned} U_{\text{em}} &= \langle \psi | \int d\mathbf{r} \hat{\mathbf{E}}(\mathbf{r}) \overline{\overline{\boldsymbol{\epsilon}}}(\mathbf{r}) \hat{\mathbf{E}}(\mathbf{r}) | \psi \rangle - \langle \text{vac} | \int d\mathbf{r} \hat{\mathbf{E}}(\mathbf{r}) \overline{\overline{\boldsymbol{\epsilon}}}(\mathbf{r}) \hat{\mathbf{E}}(\mathbf{r}) | \text{vac} \rangle \\ &= 2 \int d\mathbf{r} \mathbf{e}_j^*(\mathbf{r}) \overline{\overline{\boldsymbol{\epsilon}}}(\mathbf{r}) \mathbf{e}_j(\mathbf{r}) \\ &= 2V_{\text{eff}} \max[\mathbf{e}_j^*(\mathbf{r}) \overline{\overline{\boldsymbol{\epsilon}}}(\mathbf{r}) \mathbf{e}_j(\mathbf{r})]. \end{aligned} \quad (5)$$

Assuming a maximum field amplitude inside the isotropic dielectric with index  $\epsilon_{\text{diel}}$ , and  $U_{\text{em}} = \hbar\omega_j$ , we obtain the maximum single-photon field

$$\max[|\mathbf{e}_j(\mathbf{r})|] = \sqrt{\frac{\hbar\omega_j}{2V_{\text{eff},j}\epsilon_{\text{diel}}}}, \quad (6)$$

where we have defined the effective mode volume for mode  $j$  to be

$$V_{\text{eff},j} = \frac{\int d\mathbf{r} \mathbf{e}_j^*(\mathbf{r}) \overline{\overline{\boldsymbol{\epsilon}}}(\mathbf{r}) \mathbf{e}_j(\mathbf{r})}{\max[\mathbf{e}_j^*(\mathbf{r}) \overline{\overline{\boldsymbol{\epsilon}}}(\mathbf{r}) \mathbf{e}_j(\mathbf{r})]}. \quad (7)$$

In many of the structures demonstrated in this work, the maximum field amplitude for a single photon can be surprisingly large, reaching values of  $10^5$  V/m *per photon*.

## 1.2 Mechanical waves and their quantization

Analyzing mechanical vibrations, and their quantum description in terms of phonons in a crystal lattice can be approached in two ways. The first begins with the atomic structure of the crystal, the forces sensed by each ion, and studies the motion of these

ions. The interested reader is referred to any of a wide array of excellent textbooks on condensed matter physics for such a treatment [16]. A second approach, which is less general<sup>1</sup>, as it only applies to phonons with wavelengths much longer than the atomic spacing, involves starting with an effective continuum mechanics or elastodynamics description. This is the approach we take, as the motion of single ions is not of interest in this work. This is conceptually no different than the approach taken in Section 1.1, where the macroscopic electromagnetic fields are quantized and the motion of the charges in the structure are only considered in terms of how they contribute to the electric susceptibility of the material at optical frequencies. At this continuum limit, the material is characterized by an elasticity tensor  $\bar{c}$  (a fourth-rank tensor with components  $c_{ijkl}$  which depend on the Young's modulus  $E$ , and Poisson's ratio  $\nu$ ), its density  $\rho(\mathbf{r})$ , and its dynamical state represented by a time-dependent displacement vector field  $\mathbf{Q}(\mathbf{r}, t)$  often also denoted  $\mathbf{u}(\mathbf{r}, t)$  in the literature.

Fundamentally, it is the strain, a measure of the local deformation in a structure which is of interest. Local deformations arise from the spatial variation of  $\mathbf{Q}(\mathbf{r}, t)$ , and are found by taking the derivative of this vector field. This total derivative is symmetrized to do away with rotations, and is represented by a unitless  $3 \times 3$  matrix with components

$$S_{ij} = \frac{1}{2} (\partial_i Q_j + \partial_j Q_i). \quad (8)$$

Stress in a structure is also a  $3 \times 3$  matrix  $T$ , which gives for every infinitesimal volume element in the structure the local forces which act on its surfaces. For a surface with normal vector  $\hat{n}$ , this force is  $T \cdot \hat{n}$ . Hooke's law, *i.e.*, the linear relationship between forces on a structure and the resulting deformation, extended to this formalism can be expressed as a linear relation between strain and stress, which is compactly stated as<sup>2</sup>

$$T_{ij} = c_{ijkl} S_{kl}. \quad (9)$$

At this point Newton's law can be used to express the acceleration of volume element due to the stress in the structure,

$$\rho \partial_t^2 Q_i = \partial_j T_{ji} = \frac{1}{2} \partial_j c_{jikl} (\partial_k Q_l + \partial_l Q_k), \quad (10)$$

leading to,

$$\rho \partial_t^2 \mathbf{Q} = (\lambda + \mu) \nabla (\nabla \cdot \mathbf{Q}) + \mu \nabla^2 \mathbf{Q}. \quad (11)$$

This equation is a full vectorial wave equation for acoustic waves in an isotropic material, where the components  $c_{ijkl}$  are reduced to  $\mu$  and  $\lambda$ , the two Lamé constants.

<sup>1</sup> In a way, this approach is more general, since it applies to non-crystalline materials as well, so long as the wavelengths are larger than the interatomic spacing.

<sup>2</sup> Summations are implied over repeated indices.

Equation can be written as an eigenvector equation much like eqn. (2):

$$\omega_j^2 \mathbf{Q}_j(\mathbf{r}) = \mathbf{L} \mathbf{Q}_j(\mathbf{r}), \quad \mathbf{L}(\cdot) = -\frac{\lambda + \mu}{\rho} \nabla(\nabla \cdot (\cdot)) - \frac{\mu}{\rho} \nabla^2(\cdot). \quad (12)$$

A solution at frequency  $\omega_j$  has a mechanical mode profile  $\mathbf{Q}_j(\mathbf{r})$ .

Quantizing the motion follows an approach similar to that used for the electromagnetic field. We define phonon creation and annihilation operators,  $\hat{b}_j^\dagger$  and  $\hat{b}_j$  respectively, for each modal solution  $\mathbf{Q}_j(\mathbf{r})$  of the equations of elasticity in the structure. The field operator is then expressed in the Heisenberg picture as

$$\hat{\mathbf{Q}}(\mathbf{r}) = \sum_j \mathbf{Q}_j(\mathbf{r}) \hat{b}_j e^{-i\omega_j t} + \text{h.c.} \quad (13)$$

To calculate the proper normalization of the field profiles, we assume a single phonon state  $|\psi\rangle = |1\rangle_j \prod_{\forall k \neq j} |0\rangle_k$  and find the expected value of additional field energy above vacuum ( $|\text{vac}\rangle = \prod_k |0\rangle_k$ ):

$$\begin{aligned} U_{\text{mech}} &= \langle \psi | \int d\mathbf{r} \dot{\mathbf{Q}}(\mathbf{r}) \rho(\mathbf{r}) \dot{\mathbf{Q}}(\mathbf{r}) | \psi \rangle - \langle \text{vac} | \int d\mathbf{r} \dot{\mathbf{Q}}(\mathbf{r}) \rho(\mathbf{r}) \dot{\mathbf{Q}}(\mathbf{r}) | \text{vac} \rangle \\ &= 2\omega_j^2 \int d\mathbf{r} \mathbf{Q}_j^*(\mathbf{r}) \rho(\mathbf{r}) \mathbf{Q}_j(\mathbf{r}) \\ &= 2m_{\text{eff}} \omega_j^2 \max[|\mathbf{Q}_j(\mathbf{r})|^2]. \end{aligned} \quad (14)$$

Here we have taken the energy to be twice the kinetic energy. It is easy to show that for a mechanical mode, half of the energy will be kinetic, and the other half potential. Assuming the energy of a phonon to be  $U_{\text{mech}} = \hbar\omega_j$ , we obtain the maximum single-phonon displacement

$$x_{\text{zpf},j} \equiv \max[|\mathbf{Q}_j(\mathbf{r})|] = \sqrt{\frac{\hbar}{2m_{\text{eff},j}\omega_j}}, \quad (15)$$

where we've defined the effective mass for mode  $j$  to be

$$m_{\text{eff},j} = \frac{\int d\mathbf{r} \mathbf{Q}_j^*(\mathbf{r}) \rho(\mathbf{r}) \mathbf{Q}_j(\mathbf{r})}{\max[|\mathbf{Q}_j(\mathbf{r})|^2]}. \quad (16)$$

Intriguingly, all the structures demonstrated in this work have a zero-point fluctuation amplitude on the order of a femtometer ( $10^{-15}$  m) regardless of their effective mass (ranging from  $10^{-18}$  –  $10^{-15}$  kg).

## 2 Photonic and phononic crystals

In the late 1980s and early 1990s, analogies between engineered structures and condensed matter systems led to the prediction of novel optical [17, 18] and mechanical [19, 20] phenomena in periodic structures patterned at the nanoscale. Initially, the focus was obtaining Purcell enhanced (or inhibited) spontaneous emission from quantum emitters via localization in such optical structures by engineering the local density of states. It was soon realized that the photonic and phononic bandgaps arising in periodic structures provide a powerful design paradigm where an engineer can simply design circuits in a periodic metamaterial by careful generation of defects [21]. Due to the presence of the bandgap, defect waveguides were predicted to exhibit excellent performance (*e.g.*, loss-less sharp bends and mitigation of cross-talk), while defect cavities with wavelength-scale localization of light were predicted and soon demonstrated.

Despite significant progress, three-dimensional crystals remain difficult to fabricate in a reliable fashion, and many of the experiments have focused on quasi-1D and 2D systems made from patterns defined in thin-films of dielectric material. These thin-films are often suspended via an under-etching of the substrate beneath. In this setting, the out-of-plane confinement of light is due to total internal reflection at the boundary between a high-index dielectric and vacuum (lack of phase matching to radiation modes), while the out-of-plane confinement of phonons follows naturally from lack of propagating phonon modes in vacuum. From here on, we focus on these thin-film structures and the quasi-1D and 2D crystals that are fabricated on them. We begin first with a review of the basic properties of guided electromagnetic and acoustic waves in simple geometries with continuous translation symmetry. The focus in Section 2.1 is understanding these guided modes before the introduction of periodicity. Periodicity gives rise to a mode structure best described by band diagrams and Bloch waves as reviewed in Section 2.2. In Section 2.3, we consider how defects engineered into a periodic structure can be used to localize light and motion effectively in the same volume. Finally, we calculate the origin and strength of interactions between such co-localized excitations in Section 2.4.

### 2.1 Symmetries of guided waves

Solutions for the electromagnetic and acoustic wave equations for quasi-1D and 2D geometries, *i.e.*, beam/rod structures and slabs respectively, can be found in a variety of excellent references [22, 23, 24, 25, 26, 21]. Here we primarily introduce a general overview of the results that are important for designing nanostructures. Symmetries of the structure can be immensely useful in characterizing the modes while avoiding the inevitable confusion surrounding historical nomenclature. They also aid in predicting the types of interactions that can occur between modes.

Consider first the reflection symmetry of a structure. A reflection operator, *e.g.*, for reflections about the  $y-z$  plane, is defined as  $\sigma_x$  with  $\sigma_x(x, y, z) \equiv (-x, y, z)$ . For

a structure that is symmetric about reflections  $\sigma_n$ , *i.e.*, one where  $\sigma_n\{\bar{\mathbf{E}}(\mathbf{r})\} = \bar{\mathbf{E}}(\mathbf{r})$ , vector fields representing physical solutions of the electromagnetic and acoustic modes of the structure can be characterized by their symmetry to be symmetric (+) or anti-symmetric (-), with  $\sigma_n\mathbf{V}^{(\pm)}(\sigma_n\mathbf{r}) = \pm\mathbf{V}^{(\pm)}(\mathbf{r})$  where  $\mathbf{V}(\mathbf{r})$  can be either  $\mathbf{Q}(\mathbf{r})$  or  $\mathbf{E}(\mathbf{r})$ . Pseudo-vectors like the magnetic field, transform in the opposite way, *i.e.*, for the magnetic field one has the vector relation  $\sigma_n\mathbf{H}^{(\pm)}(\sigma_n\mathbf{r}) = \mp\mathbf{H}^{(\pm)}(\mathbf{r})$ .

Of course, only some of the properties of the solutions of eqns. (1) and (11) can be simply predicted from the symmetries alone. We assume that the reader has some familiarity with the solutions of these wave equations in a simple homogeneous isotropic material. In particular, for a given frequency and propagation direction (taken to be along  $y$ ), Maxwell's equations permit two solutions with the same propagation vector  $\mathbf{k}$  but with differing polarizations, where for both solutions the electric field  $\mathbf{E}$ , magnetic field  $\mathbf{H}$ , and  $\mathbf{k}$  are all mutually orthogonal. These two waves propagate at the same speed, given by  $c_{\text{diel.}} = 1/\sqrt{\mu_0\epsilon_{\text{diel.}}}$ . The equations of elasticity in a homogeneous isotropic medium also permit a similar pair of solutions with  $\mathbf{Q}$  perpendicular to the propagation vector, but there exists in addition a third type of elastic wave where  $\mathbf{Q}$  is in the direction of propagation. Both types of waves have linear dispersion. The latter are called a dilatational, longitudinal, or pressure waves and have propagation velocity of  $c_l = \sqrt{(\lambda + 2\mu)/\rho}$ , while the two former solutions are often called transverse, or shear waves and have velocity  $c_t = \sqrt{\mu/\rho}$ . Here,  $\mu$  and  $\lambda$  are Lamé constants, and  $\rho$  is the density of the material [22, 24]. It is easy to see from these relations that  $2c_t^2 \leq c_l^2$ . In what follows, unless otherwise stated, we consider structures formed from an elastic material with density  $\rho = 2.329 \text{ g/cm}^3$ , Young's modulus  $E = 170 \text{ GPa}$ , and Poisson's ratio  $\nu = 0.28$ , corresponding roughly to that of isotropic Si (*i.e.*, neglecting anisotropy).

### 2.1.1 Photons in a slab

Thin-film slabs possess continuous translational symmetry in the  $x$  and  $y$  directions, and a reflection symmetry in the  $z$  direction. More specifically, we take

$$\bar{\mathbf{E}}(\mathbf{r}) = \begin{cases} \epsilon_{\text{Si}} & |z| < t/2 \\ \epsilon_0 & |z| \geq t/2 \end{cases}, \quad (17)$$

where  $\epsilon_{\text{Si}} = n_{\text{Si}}^2\epsilon_0$ , and we take the refractive index of Si to be  $n_{\text{Si}} = 3.48$ , its value in the 1500 nm wavelength band. This geometry, shown in Fig. 2, clearly satisfies both  $\sigma_x\{\bar{\mathbf{E}}(\mathbf{r})\} = \bar{\mathbf{E}}(\mathbf{r})$  and  $\sigma_z\{\bar{\mathbf{E}}(\mathbf{r})\} = \bar{\mathbf{E}}(\mathbf{r})$ . The solutions of Maxwell's equations are often characterized to be symmetric or anti-symmetric about the mirror symmetry  $\sigma_x$ . For the symmetric solutions, it follows from  $\sigma_x\mathbf{E}^{(+)}(\sigma_x\mathbf{r}) = +\mathbf{E}^{(+)}(\mathbf{r})$  and  $\sigma_x\mathbf{H}^{(+)}(\sigma_x\mathbf{r}) = -\mathbf{H}^{(+)}(\mathbf{r})$ , so that  $E_x = 0$ , and  $H_z = H_y = 0$  on the  $y-z$  plane. Due to the symmetry of the structure, these components of the electromagnetic fields are also zero at all other points. Such solutions are often called transverse magnetic (TM) or p-modes in the literature, since there is no magnetic field component in the direction of propagation ( $y$ ). Taking a propagation vector  $\mathbf{k} = k_y\mathbf{e}_y$ , and using

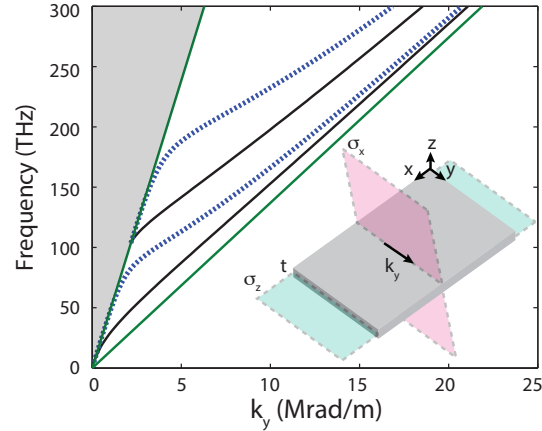


**Fig. 2** Dispersion diagram for photons in a slab with thickness  $t = 220$  nm and refractive index  $n = 3.48$  (corresponding approximately to that of Si in the  $1.5 \mu\text{m}$  wavelength band). The photonic bands were calculated by numerical solution of the determinantal equation [23]. The two lowest lying TM or p-mode bands are plotted as blue dotted curves, whereas the two lowest order TE or s-mode bands are plotted as solid black curves. The upper and lower green curves correspond to light propagation along  $e_y$  in vacuum and in a bulk material with refractive index of the slab, respectively. These are the two light lines of the slab, and the guided modes of the slab must lie in between them. The shaded grey region represents the continuum of modes which exist in the vacuum surrounding the slab.

the appropriate boundary conditions, the equations for the remaining three degrees of freedom,  $(E_z, E_y, H_x)$ , can be solved to yield a determinantal equation relating  $\omega$  and  $k_y$  [23]. The solutions anti-symmetric with respect to the transformation  $\sigma_x$  are called transverse electric (TE) or s-modes and similarly have non-zero field components  $(H_z, H_y, E_x)$ . The two lowest lying bands shown in Fig. 2 are the fundamental TE (solid) and TM (dotted) modes. The fundamental TE mode is symmetric about  $\sigma_z$ , thus  $E_z = H_x = H_y = 0$  on the  $x - y$  plane. On the  $x - y$  plane we have only non-zero  $H_z$  and  $E_x$  for the fundamental TE waves<sup>3</sup>. For an infinitely thick slab, the fundamental TE waves become the plane-wave solutions in a bulk dielectric that are linearly polarized in the  $x$  axis. Similarly, the fundamental TM waves are anti-symmetric about  $\sigma_z$ , and  $E_z$  and  $H_x$  become the only non-zero fields on the  $x - y$  plane. For an infinitely thick slab, these waves reduce to the plane wave solution of orthogonal polarization (linearly polarized in the  $z$  axis). Bands for the next higher order TE (solid) and TM (dashed) waves are also plotted in Fig. 2. These waves have the opposite symmetry about  $\sigma_z$  when compared to the fundamental modes, and thus have a node at the center of the slab.

<sup>3</sup> The optical modes of structures in this chapter arise from engineering this TE mode, and thus in the following sections we will only plot the value of  $E_x$  on the  $z = 0$  plane when representing optical mode profiles.

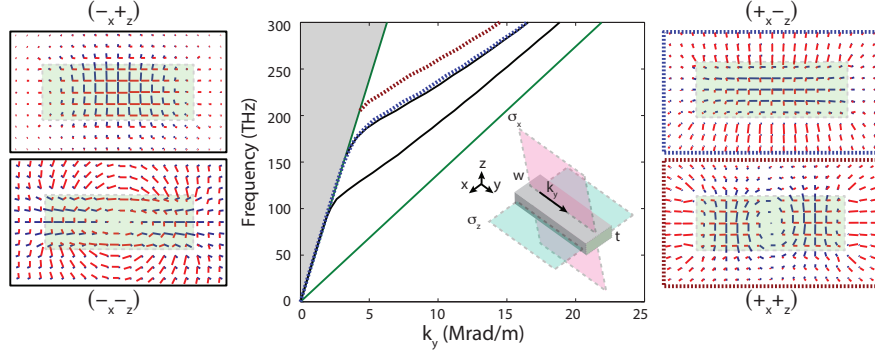


**Fig. 3** Dispersion diagram for photons propagating in a beam of Si of thickness  $t = 220$  nm and width  $w = 600$  nm, where  $x, y$  are the two transverse directions and  $y$  is the long axis of the beam along which light propagates. Also shown are transverse vector mode profile plots for the four lowest lying guided mode optical bands (along with mode symmetries) at an excitation frequency of  $\omega/2\pi = 235$  THz. Here the green region with dashed grey outline is the Si beam in cross-section, with the transverse electric field vector shown in red and the transverse magnetic field vector shown in blue. The exterior outline color and format of the mode field plots match that of the corresponding band in the band diagram. The band of interest in this work is the fundamental TE mode with symmetry  $(-x+z)$ , which as evident from the mode profile, is highly localized in the dielectric. The bands and mode profiles were calculated using a finite-difference frequency diagonalization method [27].

### 2.1.2 Photons in a beam

Beams or dielectric waveguides with rectangular cross sections have mode structures similar to slabs. The dielectric constant defining the structure is given by

$$\bar{\epsilon}(\mathbf{r}) = \begin{cases} \epsilon_{\text{Si}} & |z| < t/2, |x| < w/2 \\ \epsilon_0 & |z| \geq t/2, |x| \geq w/2 \end{cases}. \quad (18)$$

When the beam is thicker than it is wide, *i.e.*,  $t < w$ , the fundamental TM  $(+x)$  and TE  $(-x)$  guided modes of the structure are similar those of the slab. However, the field components  $(E_z, E_y, H_x)$  and  $(H_z, H_y, E_x)$ , for the TM and TE waves respectively, are the *dominant* field components, as opposed to the only non-zero field components as is the case for the slab. In some literature, these guided modes are referred to as TM- or TE-like since the magnetic or electric field are no longer truly transverse to the direction of propagation throughout the structure. The four lowest guided mode bands of a Si beam are plotted in Fig. 3 (see caption for description).

### 2.1.3 Phonons in a slab

Mechanical waves in a slab are superpositions of plane wave solutions of the bulk material, and thus share many characteristics with the three branches of acoustic

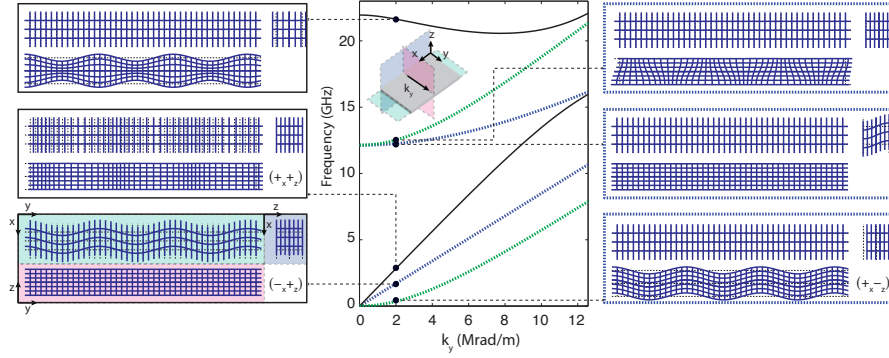


**Fig. 4** Dispersion diagram for phonons propagating in a silicon slab, or plate, of thickness  $t = 220$  nm. Here we assume Si to be an isotropic elastic material with density  $\rho = 2.329$  g/cm<sup>3</sup>, Young's modulus  $E = 170$  GPa, and Poisson's ratio  $\nu = 0.28$ . The solid black, dotted blue, and dotted green curves correspond to bands with symmetry  $(+x+z)$ ,  $(-x+z)$ , and  $(+x-z)$ , respectively. The displacement field profile for the six lowest lying phonon bands at  $k_y = 2 \times 10^6$  rad/m are also presented. The mode field plots are represented by the distortion of a uniform Cartesian grid, and shown for the  $x-y$  (top left),  $y-z$  (bottom left), and  $x-z$  (top right) planes of the structure. The vector symmetries for the three bands terminating at  $\omega = 0$  are also shown. From lowest to highest frequency, these are the flexural, horizontal shear, and extensional waves described in the text, and have vector symmetries  $(+x-z)$ ,  $(+x-z)$ , and  $(+x-z)$ , respectively. Note that the thickness of the slab (in the  $z$  direction) is exaggerated in the mode diagrams for clarity.

waves in an isotropic elastic environment despite their strong modification by the boundary conditions. For an infinite isotropic elastic material, the three types of acoustic waves with propagation vector  $\mathbf{k} = k_y \mathbf{e}_y$  can be taken to have polarizations in the  $\mathbf{e}_x$ ,  $\mathbf{e}_z$ , and  $\mathbf{e}_y$  directions. The former two are the horizontal shear (SH) and vertical shear (SV) waves, while the latter is called a pressure (P) wave. The vector symmetry of these modes with respect to  $\sigma_x$  and  $\sigma_z$  are  $(-x+z)$ ,  $(+x-z)$ , and  $(+x+z)$ , respectively, as can be deduced simply by inspection of a constant vector field with the corresponding polarization.

At a boundary with normal  $\mathbf{e}_z$ , the symmetry  $\sigma_z$  is broken, while  $\sigma_x$  is preserved allowing for a coupling between SV and P modes. Thus, the modes of a slab, which possess two such boundaries, are either linear combinations of SH plane waves, or linear combinations of SV and P waves. The first few bands for waves in a plate are shown in Fig. 4. The modes related to the SH waves are easiest to understand as they share many properties with the corresponding plane wave solutions (including the symmetry  $(-x+z)$ ). The dispersion of these modes is found to be  $\omega_{\text{SH},m}(k_y) = c_t \sqrt{k_y^2 + (m\pi/t)^2}$ , where  $c_t$  is the velocity of SH (and SV) waves in the bulk, and  $m$  is the mode number.

The combined SV and P modes form a pair of solutions called the Rayleigh-Lamb solutions for waves in a plate. These two solutions are often called 'extensional'  $(+z)$  and 'flexural'  $(-z)$ . There is no simple analytic form for the dispersion of these waves, but a calculation leads to a pair of determinantal equations describ-

ing their dispersion [24]. A property of these waves that distinguishes them from the plane wave solutions is their low energy dispersion. Because of the coupling induced between the SV and P waves, and the fact that they both go to the origin on the band diagram, the dispersion near  $\omega, k \approx 0$  is strongly modified by level repulsion. The symmetric Rayleigh-Lamb solution, *i.e.*, the extensional band  $(+x+z)$ , continues to have linear dispersion at the origin, while the dispersion of the flexural band  $(+x-z)$  is quadratic to lowest order, becoming linear again at larger wave numbers where the frequencies of the two Rayleigh-Lamb waves diverge. The low-energy expansion for the dispersion can be calculated and for the fundamental extensional wave is given by  $\omega_e(k) = c_e k$ , with  $c_e = c_t/c_l \sqrt{c_l^2 - c_t^2}$ . For the flexural wave, we find that near  $\omega, k = 0$ ,  $\omega_f(k) = c_f k^2$ , with  $c_f = t c_t \sqrt{(c_l^2 - c_t^2)/3c_l^2}$  to lowest order.

#### 2.1.4 Phonons in a beam

The solutions for mechanical waves in a beam can be mostly understood by considering waves in a plate. Due to the addition of the boundaries normal to  $e_x$ , the SH waves are also strongly modified, and will behave in a manner similar to the flexural bands of the plate. Therefore, there are two flexural modes of the beam, one polarized along the  $x$  direction with symmetry  $(-x+z)$ , and the other along the  $z$  direction with symmetry  $(+x-z)$ . Both exhibit quadratic dispersion at low energy as shown in Fig. 5. The ‘extensional’ wave in the plate corresponds to a similar wave in the beam with symmetry  $(+x+z)$  and also has linear dispersion at low energies.

There is however a fourth type of wave arising in a beam that is not analogous to any bulk or plate wave, but perhaps most closely related to SH waves in a plate. This solution to the equations of elasticity is called a ‘torsional’ wave and has symmetry  $(-x-z)$ . It is well known that there are no rotational waves in bulk media [22]. An intuitive way to see this involves considering very low energy excitations of a beam and comparing to those of a plate. At a frequency close to zero, with the wavelength going to infinity, the three bands of plate waves simply reduce to displacements of the plate in the three directions. For a beam, the fourth band corresponds of a rotation of the beam about its longitudinal axis. This rotation does not constitute a low-energy degree of freedom for the plate, since for any rotation, no matter how small, there is always a distance away from an axis of the rotation where the induced displacement vector  $\mathbf{Q}(\mathbf{r})$  becomes infinitely large. Thus it is the finite transversal extent of the beam that allows torsional modes to exist – they are a product of the boundary conditions. The existence of torsional waves in beams, which are symmetry mismatched to bulk and plate waves has been used to create mechanical resonators with extremely low clamping losses, since acoustic radiation away from the beam is prohibited by a symmetry mismatch [28, 29, 30].

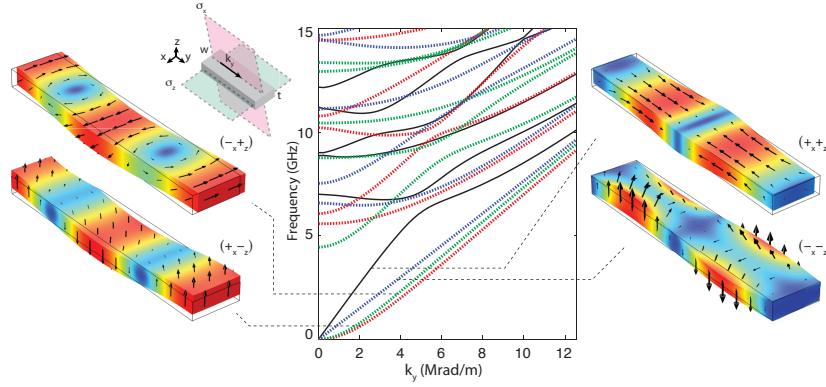


**Fig. 5** Dispersion diagram for phonons propagating in a silicon beam of thickness  $t = 220$  nm and width  $w = 600$  nm. Here we assume Si to be an isotropic elastic material with density  $\rho = 2.329$  g/cm<sup>3</sup>, Young's modulus  $E = 170$  GPa, and Poisson's ratio  $\nu = 0.28$ . The solid black, dotted blue, dotted green, and dotted red curves correspond to bands with symmetry  $(+x+z)$ ,  $(-x-z)$ ,  $(-x+z)$ , and  $(+x-z)$ , respectively. Mode plots for the four lowest lying bands which terminate at  $\omega = 0$  are also shown for wavevector  $k_y = 2 \times 10^6$  rad/m. In these mode plots the displacement of the beam from its reference form (solid black outline) is shown by the colored beam, and where red (blue) corresponds to regions of large (zero) displacement magnitude and the black vectors indicate the magnitude and direction of the displacement. The bands and mode profiles were calculated using the FEM software package COMSOL [12].

## 2.2 Introducing periodicity: band diagrams

Waves in periodic structures are best understood in terms of band theory. Bloch's theorem states that in a structure with periodic variation, the time-harmonic solutions to the optical and mechanical wave equations can be expressed as a product of a plane-wave solution ( $e^{i\mathbf{k}\cdot\mathbf{r}}$ ) and a function ( $\mathbf{e}_{\mathbf{k}}(\mathbf{r})$  or  $\mathbf{Q}_{\mathbf{k}}(\mathbf{r})$ ) possessing the same periodicity as the crystal<sup>4</sup>,

$$\mathbf{e}(\mathbf{r}) = \mathbf{e}_{\mathbf{k}}(\mathbf{r})e^{i\mathbf{k}\cdot\mathbf{r}} \quad \text{and} \quad \mathbf{Q}(\mathbf{r}) = \mathbf{Q}_{\mathbf{k}}(\mathbf{r})e^{i\mathbf{k}\cdot\mathbf{r}}. \quad (19)$$

These solutions are for a given frequency, and the vector  $\mathbf{k}$  is well-defined modulo a reciprocal lattice vector  $\mathbf{G}$ . For complex geometries, numerical methods are used to calculate the relation between  $\mathbf{k}$ , the wave vector, and  $\omega_n(\mathbf{k})$ , the frequency of the Bloch wavefunctions of band  $n$ . Using a package such as COMSOL [12] or MPB [13], we find the eigenfrequencies of the desired wave equation for a unit-cell of the crystal. Boundary conditions determining the wavevector of interest are used. It is possible to set for example a boundary condition such as  $\mathbf{Q}(\mathbf{r})|_{\partial_1} = \mathbf{Q}(\mathbf{r} + \mathbf{a})|_{\partial_2}e^{i\mathbf{k}\cdot\mathbf{a}}$  where  $\partial_{1,2}$  are two of the boundaries of the unit-cell

<sup>4</sup> We refer the reader to a text on condensed matter physics [16] for a completely analogous treatment of these concepts for electrons.

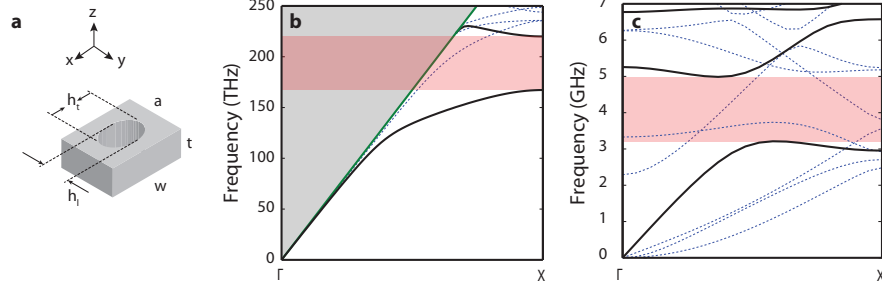


**Fig. 6** **a**, Unit cell of a quasi-1D crystal formed in a Si nanobeam. The unit-cell contains a hole shaped like an oval, with the transverse and longitudinal radii of the hole given by  $h_t = 0.76a$  and  $h_l = 0.54a$ , respectively, and the lattice constant equal to  $a = 448$  nm. **b**, Photonic band diagram of the Si nanobeam. Here we take Si to be an isotropic dielectric with refractive index  $n = 3.48$ . The fundamental TE-like band with symmetry  $(-x+z)$  is shown as a solid black curve, while the other bands are shown as blue dotted curves. The solid green curve is the vacuum light line, and the gray shaded region denotes the region with a continuum of radiation modes. The orange shaded region represents a quasi-bandgap for guided optical modes of symmetry  $(-x+z)$ . **c**, Phononic band diagram of the Si nanobeam. Here we assume Si to be an isotropic elastic material with density  $\rho = 2.329$  g/cm<sup>3</sup>, Young's modulus  $E = 170$  GPa, and Poisson's ratio  $\nu = 0.28$ . The  $(+x+z)$  bands corresponding to the extensional modes of the beam are shown as black curves, with the bands of other symmetry shown as blue dotted curves. The orange shaded region corresponds to an acoustic mode bandgap for modes of symmetry  $(+x+z)$ . In both plots, the point  $\Gamma$  refers to  $k = 0$  and  $X$  to  $k = \pi/a$  in the  $y$ -direction.

separated by a lattice vector  $\mathbf{a}$ . With such a boundary condition, the eigenfrequencies and eigenvectors of the structure are calculated, giving a set of frequencies and wavefunctions  $\{\omega_n(\mathbf{k}), Q_{\mathbf{k},n} e^{i\mathbf{k}\cdot\mathbf{r}} : n = 1, 2, 3, \dots\}$ . This process is repeated for a large set of  $\mathbf{k}$  values, generating a band diagram, *i.e.* a plot of  $\omega_n(\mathbf{k})$  vs.  $\mathbf{k}$ . For the quasi-1D case, where the periodicity is defined by discrete translations in only one direction, the axis is trivial to define, and the wavevectors are simply taken to be real numbers. Typically in this case, we take  $k \in [-G/2, G/2]$  with  $G = 2\pi/a$ . For the quasi-2D case, the wavevectors  $\mathbf{k}$  are 2D vectors, and thus a 1D path in  $\mathbf{k}$ -space starting from  $k = 0$  (the  $\Gamma$ -point), traversing the boundary of the First Brillouin Zone (FBZ), and coming back to the  $\Gamma$ -point is used.

### 2.2.1 Quasi-1D nanobeam optomechanical crystals

Patterning an array of holes in a suspended beam realizes a quasi-1D crystal structure. Such dielectric crystals, sometimes referred to as photonic crystal wires, have been considered for the last two decades in optics[31, 32] due to their ease of design and fabrication. Figure 6 shows the calculated band diagrams for the propagation of light and sound in such a quasi-1D nanobeam crystal structure.

The band structure for photons at small values of  $k$  and at low frequencies is similar to that of photons propagating in an unpatterned beam studied in Section 2.1.2.

In such a case, the wavelength is simply too large for the electromagnetic waves to sense the periodicity of the crystal. There are two bands terminating with linear dispersion at the origin of the  $\omega - k$  diagram, corresponding to the fundamental TE-like and TM-like modes of an unpatterned beam. At close to the  $X$ -point however, strong backscattering due to Bragg reflection occurs, and the bands flatten. A splitting is induced by the periodic perturbation of the dielectric. For the geometry shown, this splitting produces a quasi-bandgap of nearly 50 THz centered around 190 THz for  $(-x+z)$  symmetry guide modes. At the  $X$ -point, the upper and lower branches of the folded  $(-x+z)$  guided mode band are called the conduction and valence bands, respectively, in analogy to the electronic bands of a semiconductor. Close to the  $X$ -point, these bands possess a quadratic dispersion.

The orange shaded region in the band diagram of Fig. 6b is not strictly a bandgap though we refer to it as such in this chapter. Rather, it is a quasi-bandgap region for the fundamental TE-like modes, protected by both mirror and discrete translation symmetries. Unlike a true bandgap, there are propagating modes that have frequencies in this region. These modes are of two types – those with a phase mismatch and those with a symmetry mismatch to the guided Bloch mode band of interest. The former can be found in the grey shaded region of Fig. 6b, where a continuum of radiation modes exist. In a perfect and infinite structure, guided waves below the vacuum light line cannot leak into radiation modes due to a momentum or phase mismatch. However, if there are defects in the dielectric along the propagation direction  $y$  (whether designed or accidental) with sufficiently large Fourier components to compensate the phase mismatch, an excitation below the light line can couple to radiation modes above the light line. A structure with a highly localized perturbation (small  $\Delta y$ ) can provide a large  $\Delta k_y$  which leads to “radiation losses” (see Section 2.3). The second set of modes that the Bloch mode of interest may couple to are those with differing symmetry found below the light line. In Fig. 6b, the dotted curve crossing through the bandgap corresponds to a guided mode with the same symmetry,  $(+x-z)$ , as the fundamental TM-like mode of the simple beam presented in Fig. 3. For this band to couple to the fundamental TE-like band requires breaking of both  $\sigma_x$  and  $\sigma_z$  mirror symmetries. In a perfect structure, one has essentially a perfect bandgap, while the introduction of nonidealities causes coupling to the out of symmetry modes and an increase in radiation or scattering losses. Introduction of engineered defects to localize the light in the bandgap will necessarily yield radiation losses. These losses can be reduced below experimentally detectable limits by smoothing the defect (increasing  $\Delta y$ ) as is studied in more detail below in Section 2.3.

A similar view emerges for the phonons in the 1D periodic structure with a few caveats. For small  $k$  and low energies, where the wavelengths are much longer than the periodicity  $a$ , four bands going through the origin correspond exactly to those discussed in Section 2.1.4. As is the case for photons, these long wavelength acoustic excitations are not strongly affected by the periodicity of the lattice and simply sense an effective medium with a modified elasticity tensor. The  $(+x+z)$  band is highlighted in black showing the emergence of a symmetry-dependent band gap spanning roughly 1.5 GHz centered at around 4 GHz. The primary difference be-

tween the phononic and photonic band diagrams are the lack of a light line and radiation modes in the case of phonons. This is because phonons do not propagate in vacuum. Thus the guided modes in the phononic bandgap region are those with differing symmetry, and we call the quasi-bandgap in this case symmetry-dependent.

### 2.2.2 Quasi-2D slab optomechanical crystals

Moving from one-dimensional to two-dimensional structures is highly desirable for certain experiments. First, there is the potential for more design freedom, as well as new opportunities in scaling and networking of systems. For example, two-dimensional arrays of optomechanical structures can give rise to novel collective phenomena not obtainable in 1D systems [5], as well as the ability to guide either light or sound by careful generation of line defects [1]. A major technical advantage to 2D slab structures is their enhanced power-handling ability. Heat generated by absorption of photons in the structure can escape more easily in a 2D setting than in 1D photonic structures [33, 34]. This becomes crucially important in low temperature experiments where quantum phenomena are more easily observed. In the mesoscopic systems under study here, and at temperatures below a few kelvin, phonon-mediated thermal transport is quantized [35]. This is a particularly limiting factor for 1D nanostructures when the cut-off energy of higher order propagating phonon modes  $\hbar\Omega_M$  surpasses  $k_B T_b$ . In this case, thermal phonons can be carried away through at most four channels corresponding to the four polarizations of waves studied in Section 2.1.4. In an infinite slab, even if one dimension (for example, the thickness) is “small”, there are still an infinite number of channels for guiding phonons, corresponding to waves propagating in different directions in the plane<sup>5</sup>.

Unfortunately, the phononic property of a structure essential for good heat management, *i.e.*, a large number of phonon loss channels, is diametrically opposed to the central goal of creating long-lived mechanical resonances with low acoustic radiation losses. The quantization of thermal conductance and availability of a limited number of phonon loss channels, means that on one hand, the thermal conductance of 1D structures is poor, while on the other hand, localized mechanical resonances in a 1D setting can be fairly robust against disorder. In fact, in 1D, symmetry-dependent bandgaps are sufficient for achieving large mechanical quality factors for modes of engineered defects [36, 37] because a localized mode at a specific frequency will at most couple to only a finite number of channels in the presence of disorder. In a 2D structure however, any symmetry-breaking perturbation couples a localized resonance to a much larger number of loss channels – the same channels that provide the desirably large thermal coupling to the environment.

---

<sup>5</sup> The band diagrams for phonons shown in figures 6, 7, and 8 look similar and hide this essential distinction. We remind the reader that the bands for the 2D structures represent modes along a path traversing the boundary of the FBZ, while in the band diagram for a 1D structure shown in Fig. 6, all of the points in the FBZ are represented.

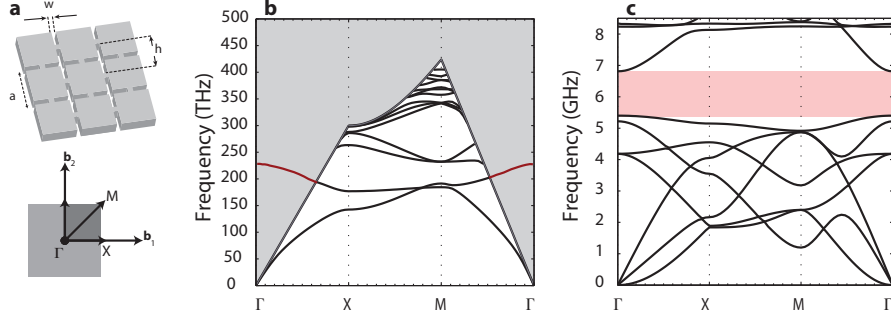


**Fig. 7** **a**, Schematic of the quasi-2D cross crystal slab structure (upper) along with its reciprocal lattice (bottom). The cross crystal structure considered here is formed from a Si thin-film of thickness  $t = 220$  nm, and consists of a periodic array of cross-shaped holes etched into it with parameters  $h = 0.8a$ ,  $w = 0.2a$ , and  $a = 500$  nm. Here we assume the Si thin-film to be an isotropic dielectric with refractive index of  $n = 3.48$  and an isotropic elastic material with  $\rho = 2.329$  g/cm<sup>3</sup>,  $E = 170$  GPa, and  $\nu = 0.28$ . **b**, Photonic band diagram, showing only the (+<sub>z</sub>) symmetry bands. The gray shaded region denotes the vacuum light cone region with a continuum of radiation modes. Leaky bands in the vacuum light cone are shown in red, and cause there to be no usable photonic bandgap. **c**, Phononic band diagram, showing the acoustic bands of all symmetries. This structure exhibits a large bandgap centered at roughly 6 GHz for all possible acoustic waves (orange shaded region). The photonic and phononic band diagrams are both plotted along the  $\Gamma \rightarrow X \rightarrow M \rightarrow \Gamma$  path in reciprocal space.

A structure possessing a *full phononic bandgap*, *i.e.*, a bandgap for all acoustic excitations regardless of their symmetry, provides the best of both worlds. A localized mechanical resonance with a frequency in the bandgap of such a crystal can be long-lived even under modest amounts of fabrication disorder. Additionally, since the thermal distribution of phonons is spectrally broad, phonon modes outside the bandgap provide a large thermal conductance to dissipate heat. Luckily, full phononic bandgaps are obtainable in thin-film nanostructures by patterning crystals with particular unit cell geometries. Perhaps even more surprisingly, it is possible to create simultaneously a full bandgap for phonons and a quasi-bandgap for guided mode photons as will be shown below for the snowflake lattice.

For a square lattice, an array of cross-shaped holes etched into a thin-film of Si can have a full phononic bandgap [38]. Each cross has a height  $h$  and a width  $w$ , which along with the lattice spacing  $a$  and slab thickness  $t$ , serve to fully define the geometry of the crystal. The reciprocal space representation of the lattice is shown in Fig. 7b, in which the common notation of the high symmetry points of the FBZ in a square lattice are used. The phononic bandstructure, including all symmetries of vibrational modes of the cross substrate is shown in Fig. 7c. For the plotted parameters, the Si structure has a bandgap between 5.3 and 6.8 GHz. This bandgap can be understood to arise due to the presence of small bridges between the connecting interconnected squares in the lattice [38]. For frequencies approaching the internal resonance frequencies of the squares, the wave propagation in the structure can be understood in a tight-binding picture. These tight-binding bands flatten as the near-

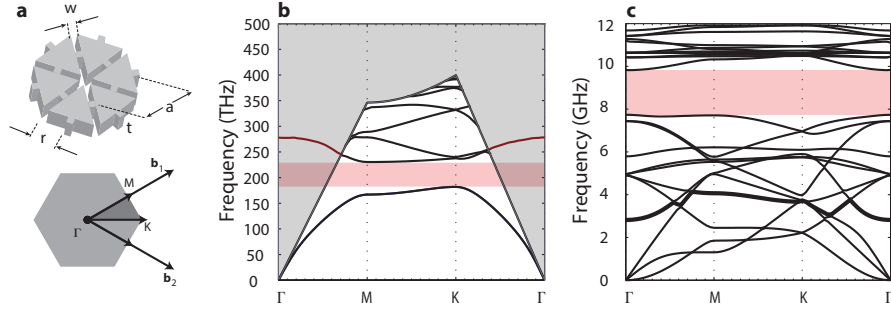


**Fig. 8** **a**, Schematic of the quasi-2D snowflake crystal slab structure (upper) along with its reciprocal lattice (bottom). The snowflake crystal structure considered here is formed from a Si thin-film of thickness  $t = 220$  nm, and consists of a periodic array of snowflake-shaped holes with parameters  $r = 0.4a$ ,  $w = 0.15a$ , and  $a = 500$  nm. Here we assume the Si thin-film to be an isotropic dielectric with refractive index of  $n = 3.48$  and an isotropic elastic material with  $\rho = 2.329$  g/cm<sup>3</sup>,  $E = 170$  GPa, and  $\nu = 0.28$ . **b**, Photonic band diagram, showing only the  $(+z)$  symmetry bands. The gray shaded region denotes the vacuum light cone region with a continuum of radiation modes. Leaky bands in the vacuum light cone are shown in red, and do not enter the region of the photonic quasi-bandgap. **c**, Phononic band diagram, showing the acoustic bands of all symmetries. This structure exhibits a large bandgap centered at roughly 9 GHz for all possible acoustic waves (orange shaded region). The photonic and phononic band diagrams are both plotted along the  $\Gamma \rightarrow M \rightarrow K \rightarrow \Gamma$  path in reciprocal space.

est neighbor interaction is made smaller by reducing the width of the connecting bridges, giving rise to a bandgap.

Photons in this structure are better described in a plane-wave expansion approach as opposed to the tight-binding picture. The square lattice, with its low symmetry, behaves differently for plane waves propagating in different directions such as at the high symmetry  $X$  and  $M$  points of the FBZ boundary. This results in a much smaller in-plane photonic bandgap for the square lattice in comparison to a higher symmetry lattice such as the hexagonal lattice. The photonic bands for the cross structure are shown in Fig. 7c for  $(+z)$  symmetry (these modes include the fundamental TE-like bands). Unfortunately, due to the presence of a *leaky* guided mode resonance in the continuum of radiation modes, no photonic bandgap is present. The leaky resonance has a large local density of states in the slab, making localized photonic states highly susceptible to leakage in the presence of fabrication disorder. Thus, the cross substrate is ruled out as a suitable structure from which to form important photonic elements such as ultrahigh- $Q$  optical cavities. Nonetheless, the simple design and full phononic bandgap of cross substrates has permitted their utilization as phonon “shields” in a variety of optomechanical experiments [39, 6, 7, 8, 10, 40].

The hexagonal lattice counterpart of the quasi-2D cross substrate is shown in Fig. 8, which we term the “snowflake” substrate. Each snowflake pattern has a radius  $r$  and a width  $w$ , which along with the lattice spacing  $a$  and slab thickness  $t$ , define the crystal geometry. Due to the higher symmetry of the hexagonal lattice, wavevectors at the high symmetry  $M$  and  $K$  points on the boundary of the FBZ sense a more

similar medium preserving the photonic bandgap. In principle, using photonic cavity design techniques outlined in Section 2.3, the quasi-2D snowflake crystal substrate can support high- $Q$  co-localized optical and mechanical resonances [41].

### 2.3 *Breaking periodicity: localized states in optomechanical crystals*

Any mechanical resonance with an eigenfrequency inside a full bandgap will be long-lived. Since phonons do not propagate in vacuum and there is no continuum of radiation modes outside of the thin-film, phononic cavities with high quality factors are easy to create, and can be defined by incorporating a defect into a quasi-2D phononic crystal slab. For example, one need only surround an area in the slab with a full bandgap phononic crystal like the cross structure presented above [39] to obtain long-lived phononic cavity resonances. The internal resonances of the surrounded region, cannot couple to any propagating leakage channel as long as the defect frequency is within the bandgap, and thus the quality factors of such resonators are not limited by clamping or radiation losses.

As explained in Section 2.2.1, the situation for photons is more complicated. The photonic bandgaps obtained in the thin-film systems are protected by phase matching and symmetries. By designing a structure so the vertical symmetry  $\sigma_z$  is conserved, coupling between TE-like and TM-like modes can be eliminated. On the other hand, to localize the field, a defect must be introduced breaking the translational symmetry of the structure and inducing coupling to the continuum of radiation modes, which leads to radiation losses. It was discovered nearly a decade ago that radiation losses can be greatly reduced in thin-film photonic crystal cavities by engineering defect modes with narrow momentum-space distributions [42, 43]. The essential idea is to generate a *smooth* defect. For these defects, modifications to the unit cell of the crystal are small enough that they can be described by a locally modified band picture. By slightly modifying a parameter, such as the radius or shape of a hole or the lattice constant, bands can be “pushed” into a bandgap, as shown in Figs. 9a-d. Surprisingly, even defects small enough to confine light in a nearly diffraction-limited volume can be designed to yield quality factors larger than  $10^6$  [44]. In Si, quality factors beyond  $10^6$  are often limited by other loss mechanisms [45].

#### 2.3.1 Nanobeam optomechanical crystal cavities

Designs for photonic nanobeam cavity resonators with very large quality factors (exceeding  $10^6$ ) were realized in Ref. [47, 48, 49] with experimental demonstrations following shortly [50]. Quasi-1D nanobeam optomechanical crystal cavities were realized by Eichenfield *et al.* [36] following very similar principles. The extra complication in the design of optomechanical crystal cavities is that the perturbation

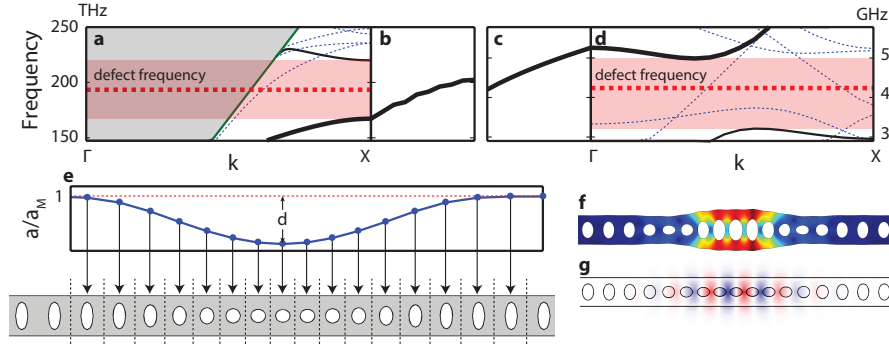


**Fig. 9** Zoomed-in region of the **a**, photonic and **d**, phononic band diagrams of Fig. 6. The guided mode optical and acoustic bands from which the localized defect states are formed are shown as thick black curves. The resulting optical and acoustic defect mode frequency is shown as a dashed red curve in both diagrams. **e**, Schematic view of the nanobeam defect cavity in the  $x$ - $y$  plane, showing the variation of the unit cell along the length of the nanobeam. **b**, The frequency of the  $X$ -point optical mode of interest as a function of unit cell perturbation. Moving from left to right on the plot corresponds to moving from the mirror region at the end of the nanobeam to the center of the defect cavity. **c**, For the same perturbation, the frequency of the  $\Gamma$ -point mechanical mode of interest. **f**, **g**, Plot of the FEM-simulated lowest order defect modes for the phonons ( $\mathbf{Q}$ ) and photons ( $E_x$ ) in the resulting defect cavity. Further details of the cavity design can be found in Ref. [46].

of the crystal must push both the optical and mechanical bands edges into their respective bandgaps. The sections of the band diagrams of interest for the nanobeam geometry are shown in Fig. 9a and d for the optics and mechanics, respectively. The defect's perturbation must then increase the optical frequency as evident from Fig. 9a, since the optical defect state is formed from the valence band's  $X$ -point Bloch function.  $\Gamma$ -point optical resonances are unsuitable as they are embedded in a continuum of radiation modes and are usually leaky.

Since the mechanical field  $\mathbf{Q}(\mathbf{r})$  enters the optomechanical coupling calculation linearly as opposed to quadratically (see Section 2.4), cancellations can occur in the overlap integral due to sign changes in the displacement field. Thus, the selection of the band edge for the mechanical resonance requires consideration of the translational and mirror symmetries of the mode. In particular, a mode taken from the  $\Gamma$ -point is preferred<sup>6</sup> since for  $X$ -point mechanical resonances the optomechanical coupling from consecutive cells for a mechanical mode with symmetry  $(+)_y$  approximately cancels, leading to a reduced optomechanical coupling rate [38]. Additionally, the only mechanical mode symmetry giving a nonzero value for the integral

<sup>6</sup> It is possible to generate mechanical modes with nonzero optomechanical coupling that do not have the "correct" Bloch function  $\sigma_y$  mirror symmetry (e.g. the 'accordion' modes demonstrated in Ref. [36]). However, a higher order resonance of the defect must be used. We do not consider these designs here as they generally have lower optomechanical coupling rates than fundamental modes formed from  $\Gamma$ -point Bloch functions with  $(+)_y$  symmetry.

in eqn. (23) is  $(+x+z)$ . The  $(+x+y+z)$   $\Gamma$ -point phonon mode with the lowest frequency lies above a symmetry dependent bandgap. Hence the defect perturbation must reduce the frequency of this  $\Gamma$ -point phonon mode.

A perturbation of the nanobeam quasi-1D crystal that satisfies both the optical and mechanical conditions is one where both the radii and the inter-hole spacing is changed, as shown schematically in Fig. 9e. The exact form of this defect is described in Ref. [46]. Under such a perturbation, the valence band  $X$ -point photonic mode is pushed to higher frequencies in the center of the nanobeam (Fig. 9b) while the  $\Gamma$ -point phononic mode is reduced in frequency (Fig. 9c). The exact defect parameters are found through numerical optimization over hundreds of simulations used to optimize a fitness function approximately related to  $g_0^2/\kappa$  [46]. The colocalized mechanical and optical resonances of the resulting optimized nanobeam defect cavity are shown in Figs. 9f and g, respectively.

### 2.3.2 Snowflake optomechanical crystal cavities

The design of cavities in a thin-film snowflake substrate follows generally the same principles as for the quasi-1D nanobeam cavity, with only a few caveats and complications. As a first step, we convert the quasi-2D crystal into an effective quasi-1D crystal by introduction of a line defect that possesses symmetry-protected optical and mechanical bandgaps. In addition to simplifying the design, this step embeds the band edge of interest in a region of frequency space with very low density of states, *i.e.* deep inside the bandgap region (essentially the same recipe has been used to create optical resonances of very high  $Q$  in a similar hexagonal lattice [44]). Next, we focus on the bands of the waveguide that provide the best optomechanical coupling estimated from an overlap integral of the optical and mechanical Bloch functions [38]. For a snowflake substrate with  $(r, w) = (0.42, 0.15)a$ ,  $t = 220$  nm, and  $a = 540$  nm, a waveguide width of  $W = 0.4a$  was found to produce strongly coupled optical and mechanical waveguide modes (see Fig. 10a). These bands are tuned into the bandgap regions in a manner analogous to that described above for the nanobeam structures. A local reduction of the radius of snowflakes causes both the mechanical and optical band edges to tune into their respective bandgaps, as elaborated in Ref. [38]. An exaggerated defect cavity in the snowflake substrate is shown in Fig. 10. In the actual cavity structure, the perturbation of the snowflake radius due to the defect is only 3%, and is spread over  $N_d = 14$  unit cells. The snowflake defect cavity was not found through numerical optimization as in the nanobeam case due to the higher complexity of the structure and the impracticality of running a large number of simulations. Instead, the design of the quasi-2D snowflake cavity involved first optimizing the waveguide unit cell optomechanical coupling, and then forming the cavity with a simple harmonic defect perturbation [38]. The mode profiles of the strongly coupled optical and mechanical modes are shown in Fig. 10. The very small perturbation needed to localize the defect cavity modes has implications for how such structures are affected by fabrication imperfections as described in Section 3.3.2).

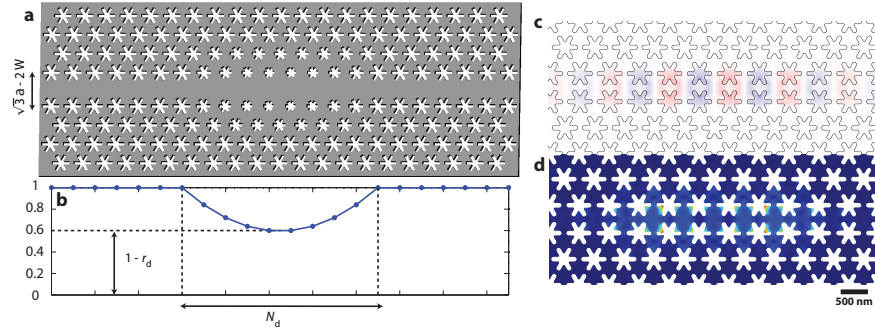


**Fig. 10** **a**, Schematic illustration (in the  $x$ - $y$  plane) of a defect cavity in the quasi-2D snowflake substrate. A linear waveguide along the  $y$ -direction ( $\Gamma$ - $K$  direction in reciprocal space) is first formed by removing a linear array of snowflake holes and shrinking the waveguide width by  $2W$ . Over  $N_d^{\text{WG}} = 7$  rows going out from the center of the waveguide, the snowflake radii are scaled quadratically from  $r(1 - r_d)$  at the center to a nominal value of  $r$ . A cavity is formed from this waveguide by then varying the parameter  $r_d$  quadratically along the axis of the waveguide over  $N_d$  lattice periods. **b**, A plot of the central waveguide hole radii along the length of the waveguide for  $N_d = 10$  and a maximum  $r_d$  at the cavity center of 0.4. Plot of the FEM simulated **c**, optical field ( $E_x(\mathbf{r})$ ) and **d**, magnitude of the mechanical displacement field ( $\mathbf{Q}(\mathbf{r})$ ) for the co-localized resonances of a defect cavity formed in a Si snowflake substrate with parameters  $(t, r, w, a) = (220, 210, 75, 500)$  nm,  $N_d^{\text{WG}} = 5$ ,  $N_d = 14$ , and  $r_{d,\text{max}} = 0.03$ . For these parameters the mechanical resonance is at a frequency of  $\nu_m = 9.50$  GHz and the optical mode at a wavelength of  $\lambda_0 = 1.459$   $\mu\text{m}$ . The theoretical vacuum optomechanical coupling rate between these modes is  $g_0/2\pi = 292$  kHz. See Ref. [38] for further details.

## 2.4 Optomechanical coupling

Given a numerically computed optical and mechanical mode, the optomechanical coupling rate between the two modes can be calculated using perturbation theory. Physically, the optomechanical coupling arises from the shift in the optical cavity frequency by the mechanical deformation. In a dielectric structure characterized by  $\bar{\epsilon}_0(\mathbf{r})$ , modifications due to deformations can be taken into account with the expression

$$\bar{\epsilon}(\mathbf{r}) = \bar{\epsilon}_0(\mathbf{r}) + \bar{\delta\epsilon}(\mathbf{r}). \quad (20)$$

To first order, such a modification of the dielectric causes a shift in the optical resonance frequency of a mode with mode profile  $\mathbf{e}(\mathbf{r})$  of

$$\omega^{(1)} = -\frac{\omega_0}{2} \frac{\langle \mathbf{e} | \bar{\delta\epsilon} | \mathbf{e} \rangle}{\langle \mathbf{e} | \bar{\epsilon}_0 | \mathbf{e} \rangle}, \quad (21)$$

where

$$\langle \mathbf{a} | \bar{\mathbf{b}} | \mathbf{c} \rangle = \int \mathbf{a}(\mathbf{r}) \cdot \bar{\mathbf{b}}(\mathbf{r}) \cdot \mathbf{c}(\mathbf{r}) d^3\mathbf{r}. \quad (22)$$

Numerical evaluation of this integral can be simplified depending on the form of  $\bar{\delta\boldsymbol{\varepsilon}}(\mathbf{r})$ . Below we consider dielectric perturbations arising from moving boundaries and the photoelastic effect.

#### 2.4.1 Boundary perturbation

A deformation of the optical resonator affects the dielectric tensor at the boundaries between different materials. This is because the high-contrast step profile of  $\bar{\boldsymbol{\varepsilon}}(\mathbf{r})$  across a boundary is shifted by deformations of the structure. By relating a deformation to a change in the dielectric constant, we can use eqn. (21) to calculate the optomechanical coupling. Johnson has derived a useful expression [51] for this shift in frequency, which when adapted to optomechanics [37], gives a frequency shift per unit displacement of

$$g_{\text{OM,Bnd}} = -\frac{\omega_0}{2} \frac{\int (\mathbf{Q}(\mathbf{r}) \cdot \mathbf{n}) (\Delta \bar{\boldsymbol{\varepsilon}} | \mathbf{e}^\parallel|^2 - \Delta (\bar{\boldsymbol{\varepsilon}}^{-1}) | \mathbf{d}^\perp|^2) dA}{\max(|\mathbf{Q}|) \int \bar{\boldsymbol{\varepsilon}}(\mathbf{r}) | \mathbf{e}(\mathbf{r})|^2 d^3\mathbf{r}}, \quad (23)$$

for a mechanical vector displacement field  $\mathbf{Q}(\mathbf{r})$ .

#### 2.4.2 Photoelastic coupling

The photoelastic contribution to the optomechanical coupling arises from local changes in the refractive index due to strain in the structure. For a particular displacement vector  $\mathbf{Q}(\mathbf{r})$  (and the corresponding strain tensor  $\bar{\mathbf{S}}$ , see eqn. (8)), the dielectric perturbation is given by

$$\bar{\delta\boldsymbol{\varepsilon}}(\mathbf{r}) = \bar{\boldsymbol{\varepsilon}} \cdot \frac{\bar{\mathbf{p}} \cdot \bar{\mathbf{S}}}{\varepsilon_0} \cdot \bar{\boldsymbol{\varepsilon}}, \quad (24)$$

which reduces to  $\delta\varepsilon_{ij} = -\varepsilon_0 n^4 p_{ijkl} S_{kl}$  for an isotropic medium. The fourth-rank tensor  $\bar{\mathbf{p}}$  with components  $p_{ijkl}$  is called the photoelastic tensor. Often, when considering the symmetries in the atomic structure of the material, a reduced tensor is used with elements  $p_{ij}$ . At this point, a simple volume integral, such as that shown in eqn. (21), can be used to find the frequency shift for a given displacement

$$g_{\text{OM,PE}} = -\frac{\omega_0}{2} \frac{\int \mathbf{e} \cdot \bar{\delta\boldsymbol{\varepsilon}} \cdot \mathbf{e} d^3\mathbf{r}}{\max(|\mathbf{Q}|) \int \bar{\boldsymbol{\varepsilon}}(\mathbf{r}) | \mathbf{e}(\mathbf{r})|^2 d^3\mathbf{r}}, \quad (25)$$

where for  $x$  and  $y$  axes aligned along the [100] and [010] crystal directions of Si, respectively,  $\mathbf{e} \cdot \bar{\delta\boldsymbol{\varepsilon}} \cdot \mathbf{e}$  is given by [10],

$$\begin{aligned}
\mathbf{e} \cdot \overline{\delta \boldsymbol{\varepsilon}} \cdot \mathbf{e} = & -\varepsilon_0 n^4 \left[ 2\Re\{E_x^* E_y\} p_{44} S_4 + 2\Re\{E_x^* E_z\} p_{44} S_5 + \Re\{E_y^* E_z\} p_{44} S_6 \right. \\
& + |E_x|^2 (p_{11} S_1 + p_{12} (S_2 + S_3)) + |E_y|^2 (p_{11} S_2 + p_{12} (S_1 + S_3)) \\
& \left. + |E_z|^2 (p_{11} S_3 + p_{12} (S_1 + S_2)) \right]. \tag{26}
\end{aligned}$$

The components of the photoelastic tensor are for such an orientation in Si,  $(p_{11}, p_{12}, p_{44}) = (-0.094, 0.017, -0.051)$  [25].

### 2.4.3 Vacuum coupling rate

The expressions derived above give us the boundary and photoelastic components for a shift in the optical cavity frequency per unit displacement of the maximum deflection point of a deformation profile  $\mathbf{Q}(\mathbf{r})$ . A natural unit for displacement is the zero-point fluctuation amplitude. The vacuum coupling rate  $g_0$  is defined as the shift in the optical cavity frequency due to a deformation equal in amplitude to the zero-point fluctuations of a mechanical mode  $\mathbf{Q}_j(\mathbf{r})$ . We can find  $g_{0,\text{Bnd}}$  and  $g_{0,\text{PE}}$  simply by multiplying the expressions (23) and (25) by the zero-point fluctuation length  $x_{\text{zpf}} = \sqrt{\hbar/(2m_{\text{eff}}\Omega_M)}$  (see eqn. 15). The total coupling rate is then simply their sum  $g_0 = g_{0,\text{Bnd}} + g_{0,\text{PE}}$ , and the corresponding optomechanical interaction Hamiltonian can be written as,

$$\begin{aligned}
H_{\text{OM,int}} &= \hbar(g_{\text{OM,PE}} + g_{\text{OM,Bnd}}) \hat{x} \hat{a}^\dagger \hat{a} \\
&= \hbar g_0 (\hat{b}^\dagger + \hat{b}) \hat{a}^\dagger \hat{a}. \tag{27}
\end{aligned}$$

## 3 Fabrication and characterization of devices

### 3.1 Fabrication

The steps taken to fabricate the Si devices presented in this chapter are briefly summarized in Fig. 11. The starting point for device fabrication is a silicon-on-insulator (SOI) wafer, which has a thin top Si device layer ( $\sim 200$  nm) sitting on top of a buried silicon dioxide layer ( $3 \mu\text{m}$ ) which itself is atop a Si handle wafer. The fabrication procedure involves one layer of electron-beam lithography (Vistec 100 kV lithography system with ZEP-520A resist), a dry plasma etch ( $\text{SF}_6/\text{C}_4\text{F}_8$ ) to transfer the pattern into the top Si device layer, and a final wet etch (1:1  $\text{HF}:\text{H}_2\text{O}$ ) of the underlying silicon dioxide layer to create a free-standing structure. It was found that the mechanical and optical resonator quality factors were highly dependent on the final chemical etch steps in the fabrication in which the Si surfaces properties are determined. The recipe giving the best results was found to involve performing repeated Piranha (3:1  $\text{H}_2\text{SO}_4:\text{H}_2\text{O}_2$ ) cleans (600 s, stirred at 250 rpm), followed by hydrogen termination using a weak 1:20  $\text{HF}:\text{H}_2\text{O}$  solution (60 s) and a final DI

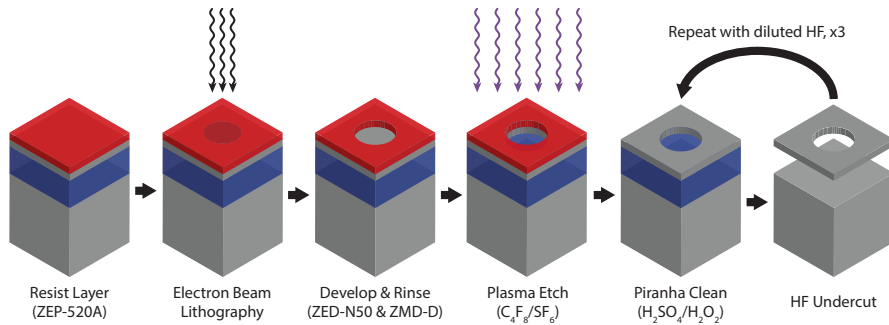


**Fig. 11** Fabrication steps for a Si OMC device fabricated from SOI. See text for process description. Figure adapted from Ref. [46].

water bath ( $30\text{ s} \times 2$ ). It is believed that such a preparation creates a stable hydrogen-terminated surface that is desirable for both the optical [45] and mechanical response of the structure.

Fabrication of the Si OMC cavities studied here benefit from highly optimized and established materials processing techniques that have been developed for the microelectronic industry and the availability of SOI wafers. Even though our focus here is on Si, similar techniques have recently been developed for materials such as diamond [52, 53, 54] and silicon carbide [55, 56], which are expected to have excellent optical and mechanical properties.

### 3.2 *Fiber-taper optical coupling and characterization*

In order to rapidly test devices on a wafer scale, we have developed an optical probing technique for micro- and nano-phonic devices that utilizes a tapered optical fiber, heated and stretched down to a diameter on the order of a micron, and in which a small dimple has been flame polished [57, 58] to allow for local device probing. The first and most simple way to use a dimpled fiber is to directly couple to an optical resonator via the tapers evanescent field. Typically, a dimpled fiber taper is mounted in a “U”-shape with the dimpled region extending at the end of the “U”, and brought into the near-field of a given optical resonator using electronically controlled stages with sub-micron-level positioning accuracy and visual feedback under a microscope. The taper is then placed in contact with the surface of the chip, close to the optical cavity, as shown in Fig. 12 for a snowflake and nanobeam OMC cavity. This induces some near field evanescent coupling between the resonator’s modes and the guided modes of the fiber. The optical resonator can be then probed in both reflection and transmission using both directions of the fiber waveguide. Such fiber coupling systems have been demonstrated in room temperature ambient conditions as well as in cryogenic vacuum environments. In air, rapid characterization

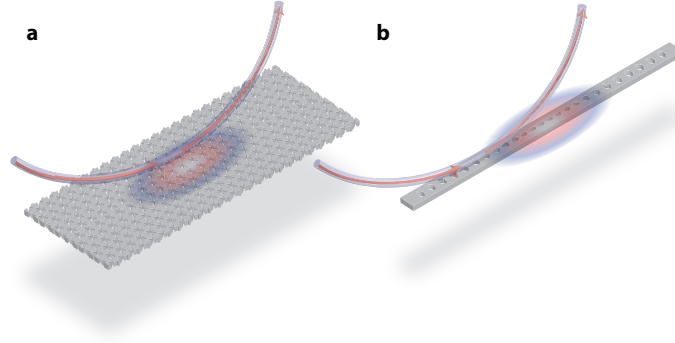


**Fig. 12** Schematic showing the alignment and placing of a dimpled fiber taper in the near field of **a**, a quasi-2D snowflake substrate cavity and **b**, a quasi-1D nanobeam cavity. This sort of coupling does not rely on phase-matching and can provide efficient bi-directional coupling to such Si OMC cavities. Note that in many cases the taper is mechanically stabilized by bringing it into contact with the surface of the chip.

of a large number of devices on a chip is possible, facilitating a quick turnaround between design, fabrication, and characterization of devices.

The type of coupling achieved using this direct fiber taper coupling scheme is bi-directional in that light from the resonator can escape into directions of the fiber taper waveguide. This so-called “two-sided coupling” is schematically illustrated in Fig. 13a. There are two propagating modes in the fiber (L and R), both of which couple to the optical resonance at a rate  $\kappa_e/2$ . The total loading of the optical cavity is then  $\kappa = \kappa_e + \kappa_i$ , where  $\kappa$  is the optical energy decay rate of the loaded cavity and  $\kappa_i$  is the intrinsic energy loss rate that consists only of the undetected optical loss channels in the system (due to scattering, absorption, and coupling to higher order parasitic guided modes of the fiber). The situation, considering only the optical degree of freedom and neglecting any optomechanical coupling, is then well described by a Heisenberg-Langevin equation,

$$\frac{d}{dt}\hat{a} = -(i\Delta + \frac{\kappa}{2})\hat{a} - \sqrt{\kappa_e/2}(\hat{a}_{in,L} + \hat{a}_{in,R}) - \sqrt{\kappa_i}\hat{a}_{in,i}, \quad (28)$$

and input-output boundary conditions,

$$\hat{a}_{out,k} = \hat{a}_{in,k} + \sqrt{\frac{\kappa_e}{2}}\hat{a}, \quad k = L, R. \quad (29)$$

Assuming that a “good” coupling has been achieved, *i.e.*, there is minimal insertion loss when the taper touches the chip and the observed transmission spectrum is flat away from the resonance, extracting the optical parameters of the system is straight-forward. A measurement of the transmitted optical power versus laser frequency results in a (undercoupled) curve resembling that shown in Fig. 13c . The

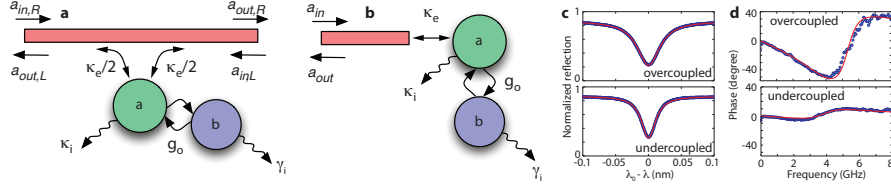


**Fig. 13** **a**, Bi-directional evanescent coupling geometry, in which the “transmitted” field goes into the forward  $a_{out}$  waveguide channel and the “reflected” field goes into the backward  $a_{out}$  waveguide channel. This is the coupling geometry we will be focusing on in this work, in which the laser input channel is  $a_{in}$  and the detection channel is the forward waveguide channel,  $a_{out}$ . **b**, Single-sided end-fire coupling geometry. This is the ideal measurement geometry since  $\kappa = \kappa_e$ , in which all of the optical signal that is coupled into the cavity can be, in principle, collected and detected in the  $a_{out}$  channel. **c**, and **d**, show the intensity and phase shift of the reflected laser light versus frequency for the over- ( $\kappa_e > \kappa$ ) and under- ( $\kappa_e < \kappa$ ) coupled cases of the single-sided cavity coupling scheme. Note that for the bi-directional coupling scheme, the transmitted light intensity and phase will be that of the undercoupled case shown in **c** and **d**.

total optical cavity decay rate  $\kappa$  can be read from linewidth, while the transmission depth  $T_d$  can be used to find  $\kappa_e/\kappa = 1 - \sqrt{T_d}$ .

The symmetric two-sided coupling achieved by direct taper coupling to the cavity has one major technical drawback when it comes to measurements in optomechanics. Considering that only one end of the waveguide is sent to the detection setup, 50% of the photons leaving the cavity are automatically lost due to the presence of the alternate unmonitored propagation direction for light in the fiber. Though it is possible in principle to fully duplicate the measurement apparatus for both channels of the waveguide and combine the results to avoid loss of information for certain measurements, it is not obvious how to extend this to all experiments (e.g., generation of squeezed light [11]). An optimal scheme would consist of coupling a single-ended waveguide to the optical cavity, such that photons leaving the cavity can only enter a single propagating mode. Such a scheme is achievable using a dimpled fiber taper with the OMC cavities studied here through the use of a two-stage-coupler as shown in Fig. 14 and detailed in recent experiments [59, 60].

In the first stage, the adiabatic mode conversion stage, the propagating mode of the fiber taper is converted into the fundamental TE mode of a nanobeam waveguide. This is accomplished by creating a region of waveguide (roughly 30  $\mu\text{m}$ ) that has tapered profile, the details of which can be found in Ref. [61]. The second stage of the adiabatic coupler consists bringing this waveguide close to the cavity to achieve the desired near-field coupling. This distance, labeled  $S$  in Fig. 14b, can be continuously varied, giving fine control over the coupling. Moreover, there is no physical contact between the coupling waveguide and the nanobeam, better isolating the mechanical resonator from loss channels. The waveguide is then terminated in a way to minimize scattering into vacuum by introducing holes that gradually increase in size, as shown in Fig. 14b. This termination eliminates one of the two directions that light can propagate out of the system, forcing the light to leave in the backward

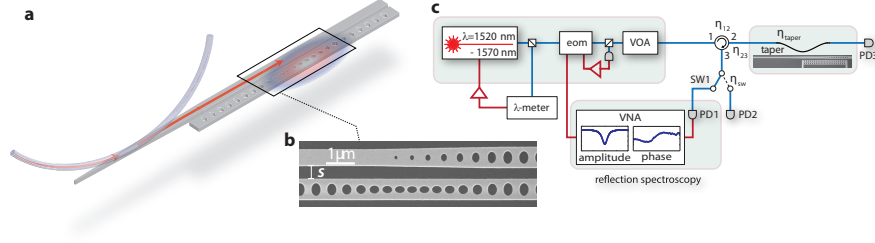


**Fig. 14** **a**, Schematic for a two-stage adiabatic taper coupler. The dimpled fiber taper is placed on a tapered Si waveguide with an effective index that crosses the fundamental mode of the fiber. **b**, The Si waveguide is brought into the near field of the OMC cavity by lithographically defining the gap  $S$ . Terminating the Si coupling waveguide with a series of holes forming a photonic crystal mirror prevents leakage of light past the OMC cavity in the transmission channel. All the light coupled radiated by the OMC cavity is then captured in the reflection channel of the Si waveguide. **c**, An experimental setup used to characterize optomechanical devices. Laser light goes through an electro-optic modulator (eom) before being coupled into the device under test, generating optical sidebands at a microwave modulation frequency. The reflected optical signal from the device is separated using a circulator and sent to a high-speed photodetector (PD1). The microwave signal from the photodetector corresponding to beating between the optical carrier and its optical sidebands is then sent into a vector network analyzer (VNA) which is also used to modulate the eom. This allows the measurement and characterization of the amplitude and phase response of an OMC cavity to a generated optical sideband near the optical cavity resonance.

propagating channel of the fiber. The Heisenberg-Langevin equations for the optical subsystem is

$$\frac{d}{dt}\hat{a} = -\left(i\Delta + \frac{\kappa}{2}\right)\hat{a} - \sqrt{\kappa_e}\hat{a}_{in,WG} - \sqrt{\kappa_i}\hat{a}_{in,i}, \quad (30)$$

where

$$\hat{a}_{out,WG} = \hat{a}_{in,WG} + \sqrt{\kappa_e}\hat{a}. \quad (31)$$

It is not possible to distinguish between overcoupled ( $\kappa_e > \kappa_i$ ) and undercoupled ( $\kappa_e < \kappa_i$ ) devices by only looking at the reflected power (see Fig. 13c). It is therefore important to consider the phase response. Optical sidebands of the laser are generated using an electro-optic modulator (labeled ‘eom’) in Fig. 14c. This sideband is swept over the cavity by changing the modulation frequency, while its phase relative to the carrier is monitored using a vector network analyzer. The sideband transmission is found to be (in the absence of the coupled mechanical response)

$$t(\Delta_{mod}) = 1 - \frac{\kappa_e}{i(\Delta - \Delta_{mod}) + \frac{\kappa}{2}}. \quad (32)$$

The resulting phase response is shown in Fig. 14e. By normalizing the phase response to a detuning far from the cavity resonance, and then fitting the normalized

phase response to the argument of  $t(\Delta_{\text{mod}})/t(0)$ , we obtain the linewidth  $\kappa$  and coupling rate  $\kappa_c$  unambiguously.

### 3.3 Characterization of mechanical properties

Having characterized the optical properties ( $\omega_{\text{opt}}$ ,  $\kappa$ , and  $\kappa_c$ ) we turn our attention to the mechanical and optomechanical properties of the system: the mechanical frequency  $\Omega_M$ , intrinsic mechanical linewidth  $\gamma_i$ , and optomechanical coupling rate  $g_0$ . These can be inferred by studying modifications to the optical cavity response due to the coupled phonon resonance. In particular, an effect akin to electromagnetically induced transparency (EIT) in 3-level atoms can be used to extract the optomechanical system parameters [62, 63, 6]. For a laser drive tuned to frequency  $\omega_L = \omega_{\text{opt}} - \Delta$ , with  $\Delta$  close to the mechanical frequency, an effective beam-splitter interaction between the optical and mechanical cavities is induced with a characteristic rate of  $G = |\alpha_0|g_0$  ( $|\alpha_0|$  is the coherent state amplitude for the driven optical resonance). A modulated sideband at two-photon detuning  $\Delta_{\text{mod}}$  will have a transmission coefficient [6]

$$t(\Delta_{\text{mod}}) = 1 - \frac{\kappa_c/2}{i(\Delta - \Delta_{\text{mod}}) + \frac{\kappa}{2} + \frac{|G|^2}{i(\Omega_M - \Delta_{\text{mod}}) + \gamma_i/2}}. \quad (33)$$

The experimental setup used to measure  $t(\Delta_{\text{mod}})$  is similar to that shown in Fig. 14c. When the modulated tone is roughly equal to the mechanical frequency, the periodically oscillating radiation pressure force induced by the beating of the sideband and the carrier drives the mechanical motion to large amplitudes, modifying the transmission of the sideband. This is the physics captured in eqn. (33). This type of mechanical characterization, used in Refs [6, 7, 10, 41], requires accurate calibration of the intracavity photon number since  $|\alpha_0| = \sqrt{n_c}$  is required to convert  $G$  to  $g_0$ .

Alternatively, with no external modulation of the carrier, the mechanical motion due to thermal noise will generate a sideband on the carrier and the power spectral density of this thermal noise can be measured by heterodyne detection of the transmitted light. This detected spectrum is Lorentzian in shape and has a linewidth of approximately  $\gamma_{\pm} = \gamma_i \pm |\Gamma_{\text{opt}}|$ ,  $|\Gamma_{\text{opt}}| \approx 4|G|^2/\kappa$  when  $\Delta = \pm\Omega_M$ , with the  $\Delta = -\Omega_M$  measurement only achievable for optical powers where  $\gamma_i > |\Gamma_{\text{opt}}|$ . By sweeping the optical power, and assuming that  $\gamma_i$  is constant, the value of  $G$  as a function of optical power can be measured. Accurate calibration of  $|\alpha_0|$  is again required for extraction of  $g_0$ . This method was used in conjunction with EIT spectroscopy in Refs [7, 10].

Finally, in cases where  $g_0$  is too small to accurately extract its value from optical modification of the mechanical linewidth, a fully calibrated thermometry procedure can be undertaken. The thermal Brownian motion power spectral density (PSD) is detected and the  $g_0$  is extracted by assuming a bath and mode temperature. Such a procedure requires precise calibration of the inefficiencies of the optical train, the

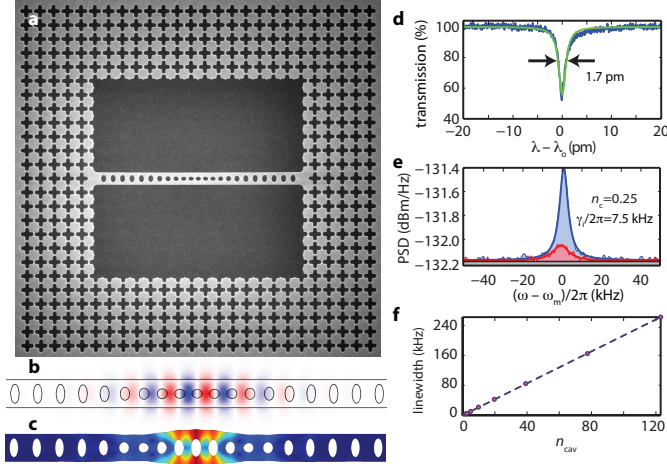


**Fig. 15** **a**, SEM image showing a cross crystal phononic shield surrounding a quasi-1D Si nanobeam OMC. FEM simulations of the strongly coupled **b**, optical and **c**, mechanical resonance mode profiles. **d**, Normalized optical transmission spectrum, centered at 1544.8 nm, showing the fundamental TE-like optical cavity mode of the nanobeam. **e**, Optically transduced thermal noise power spectral density centered at the mechanical frequency,  $\Omega_M/2\pi = 5.1$  GHz, with the input laser red-detuned (red curve) and blue-detuned (blue curve) from the cavity resonance by the mechanical frequency. **f**, Plot of the measured optically-induced mechanical linewidth ( $\Gamma_{\text{opt}}$ ) versus intra-cavity photon number ( $n_c$ ). The slope of a linear fit to the measured data (dashed curve) is used to extract  $g_0$ .

phase and intensity noise on the laser [11], as well as an accurate understanding of the gain and conversion ratios in the detector and microwave part of the setup [36, 39, 64].

### 3.3.1 Nanobeam in a phononic shield

The phononic bandgaps in the quasi-1D nanobeam OMCs studied here are symmetry-dependent, and as explained in Section 2.2.1, this leaves open channels for phonons to radiate away from the localized resonance<sup>7</sup>. By surrounding the nanobeam with a phononic crystal possessing a full phononic bandgap, such as the cross crystal introduced in Section 2.2.2, residual disorder-induced clamping losses can be eliminated from the system. Simulations taking into account disorder in the placement of the nanobeam holes show that given a certain amount of relative disorder, clamping losses can be reduced by six orders of magnitude through incorporation of a cross crystal incorporating six unit cells [46]. In experiments, we found that at cryogenic temperatures ( $\sim 10$  K), the mechanical mode quality factors of nanobeams with

<sup>7</sup> Recently 1D-OMC cavities with full phononic bandgaps have been demonstrated [65].

phononic shields were greater than those without phononic shields. The nanobeams without shields exhibited mechanical  $Q$ s not exceeding  $3 \times 10^4$ , while the shielded nanobeams had  $Q$ 's approaching  $10^6$ .

A shielded nanobeam OMC cavity, detailed in Ref. [10], is shown above in Fig. 15a. Five layers of crosses were used in the phononic shield in this experiment to help further isolate the localized cavity phonon resonance at frequency  $\Omega_M/2\pi = 5.1$  GHz from the environment. The fundamental optical resonance of the cavity at wavelength  $\lambda = 1544.8$  nm is strongly coupled to localized phonon mode. Simulated mode profiles of the coupled optical and mechanical resonances are shown in Fig. 15b and c, respectively. The nanobeam was designed in accordance to the concepts described in Section 2.3.1, and in more detail elsewhere [46]. In this design, the nanobeam cavity was optimized in a way to minimize  $g_{0,\text{Bnd}}$  in favor of a large photoelastic contribution  $g_{0,\text{PE}}$  as it was found that the signs of the photoelastic and boundary perturbation optomechanical coupling oppose each other.

The optical characterization of the device was performed using direct fiber taper coupling. From the coupling depth and the measured linewidth shown in Fig. 15d, an intrinsic optical quality factor of  $1.2 \times 10^6$  was inferred. Mechanical spectroscopy data is shown in Fig. 15e, with the PSD of the transmitted laser light recorded at around the mechanical frequency for laser-cavity detunings of  $\Delta = \pm\Omega_M$ . An intrinsic mechanical linewidth of  $\gamma_l/2\pi = 7.5$  kHz is inferred corresponding to a mechanical quality factor of  $Q_m = 6.8 \times 10^5$ . In addition the  $g_0$  is measured by varying the optical power and recording the change in linewidth. From the linear fit shown in Fig. 15f, an optomechanical coupling rate of  $g_0/2\pi = 1.1$  MHz is inferred.

### 3.3.2 Snowflake cavities and fabrication disorder

The snowflake cavities presented in Section 2.3.2 were fabricated in a thin-film Si layer [41], and their properties were measured. Direct fiber taper coupling was used to determine the optical mode  $Q$ -factor. Afterwards, two-tone ‘‘EIT’’ spectroscopy was used to understand the mechanical mode properties using a set-up similar to that shown in Fig. 14c. In this scheme the VNA outputs a microwave tone that modulates the laser beam sent to the optical cavity, creating optical sidebands. The optomechanical interaction changes the phase between the sidebands and the carrier, and the extra phase imparted on the sidebands is measured by the VNA by taking the output of the high speed photodetector. The normalized phase response of the VNA ( $\text{angle}[s_{12}(\delta)]$ ) for low and high optical input powers are shown in Figs. 16a and b, respectively, for a laser-cavity detuning of  $\Delta = \Omega_M$ . The measured spectra show two mechanical modes with frequencies at 9.309 GHz and 9.316 GHz. By varying the optical power, and fitting these measured curves to the model described in Section 3.3, the intrinsic and damped mechanical linewidth can be measured. These measurements are plotted in Fig. 16d against optical power. The linear fits of  $\Gamma_{\text{opt}}$  are used to infer a value for  $g_0/2\pi$ , which is found to be 220 kHz for the upper frequency mode and 180 kHz for the lower frequency mode.

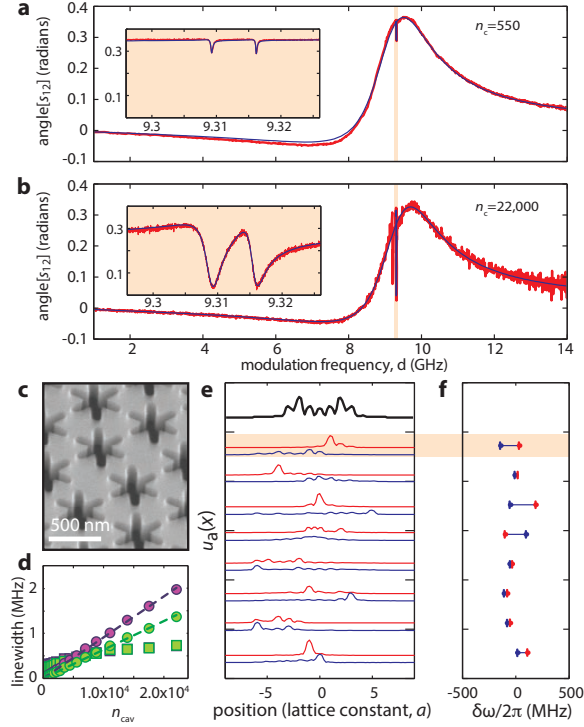


**Fig. 16** **a**, Low and **b**, high power EIT spectra of a Si quasi-2D snowflake cavity with parameters . The fits shown in the insets are used to extract the optomechanical parameters. **c**, SEM image of a fabricated snowflake OMC cavity. **d**, Plot of the resulting fit mechanical damping rates versus  $n_c$ . Measured  $\gamma$  is shown as squares and  $\Gamma_{\text{opt}}$  is shown as circles, with the low (high) frequency mode shown in green (purple). Dashed lines correspond to linear fits to the  $\Gamma_{\text{opt}}$  data. For a representative 8 of the simulated disordered structures: **e**, plot of the linear acoustic energy density profile for the two most strongly coupled mechanical resonances and **f**, plot of the corresponding mechanical frequency difference for these mechanical resonances.

The presence of two nearly-degenerate and strongly coupled mechanical resonances likely arises from the effects of disorder in the fabricated structure. The flat dispersion (low group velocity) of the mechanical waveguide mode from which the snowflake cavity resonances are formed (see Ref. [38] for a detailed study of these guided modes) causes the mechanical mode spectrum to be highly sensitive to fabrication disorder. In fact, this flat dispersion allows an engineered defect consisting of only a 3% modulation of the snowflake radius to be sufficient for localization of the mechanical mode, as described in Section 2.3.2. This extreme sensitivity to disorder makes exact determination of the mechanical mode structure from the measured spectra difficult. The simulated linear mechanical energy distribution along the length of the cavity for the two most strongly coupled mechanical modes of a series of disordered snowflake cavities is shown in Fig. 16e. In Fig. 16f we show

the corresponding frequency splitting of these two modes. Here, disorder was introduced in the simulation by varying the snowflake hole position and dimensions with a normal distribution of 2% (we expect disorder in the radii to be on the order of 1-2% from fits to SEM images). The simulated disordered structures are found to yield similar mode couplings and mode frequency splitting as that in the measured snowflake device.

## 4 Outlook and future directions

A survey of a variety of thin-film OMC cavity structures, and their measured optical, mechanical, and optomechanical coupling properties are presented in Table 1. From this table it is clear that a variety of different geometries have been realized, utilizing 1D and 2D crystal structures with partial and full phononic bandgaps. New materials have also begun to be used to create OMC structures, including piezoelectrics such as AlN which offer the promise of integrating opto-mechanical and electro-mechanical functionality into the same device. For the most part, however, optomechanical crystals have thus far been experimentally realized only as individual cavity elements. Given the chip-scale nature of thin-film optomechanical crystal devices, and the ability to “wire up” different elements via photonic or phononic waveguides, an interesting future direction will be to explore the classical and quantum properties of arrays of coupled optomechanical crystal cavities [2, 8, 4, 66, 67, 68, 5].

The quantum nonlinear regime of cavity optomechanics, which requires both sideband resolution ( $(\kappa/\Omega_M) < 1$ ) and strong quantum coupling ( $(g_0/\kappa) > 1$ ), remains completely unexplored experimentally. This regime would enable one to create quantum phononic gates for performing quantum information processing tasks, to generate non-Gaussian states of light through a photon-blockade-like effect, and to perform quantum non-demolition measurements of either photon or phonon number [69, 70, 71, 72]. As such, it is interesting to consider what the limits of optomechanical coupling in OMCs might be.

A back of the envelope estimate of the requirements needed to reach the strong quantum coupling limit can be made by considering the moving boundary contribution to the optomechanical coupling. Assuming that the spatial extent of the photon cavity resonance can be limited to roughly  $\lambda_0/n$  (where  $\lambda_0$  is the free-space optical wavelength for optical frequency  $\omega_o = 2\pi c/\lambda_0$ , and  $n$  is the refractive index of the material forming the OMC cavity), the optomechanical coupling will be roughly  $g_0/2\pi \approx (n\omega_o/\lambda_0)x_{zpf}$ . For typical solid state materials, with densities  $\rho \sim 1 \text{ g/cm}^3$  and Young’s modulus  $E \sim 100 \text{ GPa}$ , the zero-point-motion amplitude of the fundamental mechanical resonances of a given structure is approximately  $x_{zpf} \sim 1\text{-}10 \text{ fm}$ , even for the complex OMC structures studied here. For a free-space wavelength of  $1.5 \mu\text{m}$  and a refractive index of  $n = 3.5$ , this yields a  $g_0$  of approximately 2 MHz, very close to the maximum optomechanical coupling realized so far in OMCs. The corresponding ratio of vacuum coupling to optical linewidth is then,  $g_0/\kappa \sim Q_o(nx_{zpf}/\lambda_0)$ , where  $Q_o$  is the optical cavity resonance  $Q$ -factor and

	$T$ [K]	$\Omega_M/2\pi$ [GHz]	$Q_m$	$g_0/2\pi$ [kHz]	phonon confinement	material	Ref.
Eichenfield et al. (2009)	300	2	$10^3 - 10^4$	220	p1D	Si	[36]
Alegre et al. (2011)	30	1	$10^4$	60	f2D (+)	Si	[39]
Gavartin et al. (2011)	300	0.9	$10^2 - 10^3$	93	p2D	InP	[64]
Safavi-Naeini et al. (2011)	30	3.6	$10^4$	800	p1D and f2D (+)	Si	[6]
Chan et al. (2011)	20	3.7	$10^5$	800	p1D and f2D (+)	Si	[7]
Chan et al. (2012)	10	5.1	$10^6$	1100	p1D and f2D (+)	Si	[10]
Bochmann et al. (2013)	300	4.2	$10^3$	30	p1D	AlN	[75]
Safavi-Naeini et al. (2014)	10	9.3	$10^4 - 10^5$	220	f2D (*)	Si	[41]
Gomis-Bresco et al. (2014)	300	3-4	$10^3$	1200	f1D	Si	[65]

**Table 1** Survey of experimentally realized thin-film optomechanical crystal devices. Phonon confinement is obtained through full (f) and partial (p) bandgaps in quasi-1D and quasi-2D geometries. Systems using cross (+) and snowflake (\*) crystals are also indicated.

$\eta \equiv (nx_{zpf}/\lambda_0)$  is a Lamb-Dicke parameter, of order  $10^{-8}$  in the currently realized OMC cavities.

For the optimized nanobeam OMC device of Ref. [10], the optical  $Q$ -factor was measured to be as high as  $Q_o = 1.2 \times 10^6$  (limited by optical scattering and absorption), yielding a measured ratio of  $g_0/\kappa = 0.0079$ , still significantly far from the strong quantum coupling regime. One idea for increasing the optomechanical Lamb-Dicke parameter involves the use of nanoscale slots within OMC structures [73]. Similar structures have been proposed as a means in nanophotonic waveguides and cavities to generate large Purcell enhanced spontaneous emission of emitters embedded in the slot. In the case of optomechanics, nanoscale slots can be used to create extremely large electric field strengths at the material boundaries, greatly enhancing the moving boundary contribution to the optomechanical coupling. One may also seek to incorporate new materials with large photoelastic coefficients, such as GaAs, into OMCs so as to increase the attainable volume contribution to the optomechanical coupling. Further improvements in optical  $Q$  may also be expected [74], and looking to the future it will be interesting to see if this along with new clever techniques for increasing the optomechanical Lamb-Dicke parameter may be employed to reach the quantum nonlinear regime of cavity optomechanics.

**Acknowledgements** The authors would like to acknowledge the significant contributions to this work by Jasper Chan, Matt Eichenfield, Jeff Hill, Simon Gröblacher, Thiago Alegre, Alex Krause, Sean Meenehan, and Justin Cohen. The work was supported by the DARPA ORCHID and MESO programs, the Institute for Quantum Information and Matter, an NSF Physics Frontiers Center with support of the Gordon and Betty Moore Foundation, and the Kavli Nanoscience Institute at Caltech. ASN gratefully acknowledges support from NSERC.

## References

1. A.H. Safavi-Naeini, O. Painter, New J. Phys. **13**, 013017 (2011)

2. D. Chang, A.H. Safavi-Naeini, M. Hafezi, O. Painter, *New J. Phys.* **13**, 023003 (2011)
3. G. Heinrich, M. Ludwig, J. Qian, B. Kubala, F. Marquardt, *Phys. Rev. Lett.* **107**(4), 043603 (2011)
4. M. Schmidt, M. Ludwig, F. Marquardt, *New Journal of Physics* **14**(12), 125005 (2012)
5. M. Schmidt, V. Peano, F. Marquardt, arXiv:1311.7095 (2013)
6. A.H. Safavi-Naeini, T.P.M. Alegre, J. Chan, M. Eichenfield, M. Winger, Q. Lin, J.T. Hill, D. Chang, O. Painter, *Nature* **472**, 69 (2011)
7. J. Chan, T.P.M. Alegre, A.H. Safavi-Naeini, J.T. Hill, A. Krause, S. Gröblacher, M. Aspelmeyer, O. Painter, *Nature* **478**, 89 (2011)
8. A.H. Safavi-Naeini, J. Chan, J.T. Hill, T.P.M. Alegre, A. Krause, O. Painter, *Phys. Rev. Lett.* **108**(3), 033602 (2012)
9. J.T. Hill, A.H. Safavi-Naeini, J. Chan, O. Painter, *Nature Communications* **3**, 1196 (2012)
10. J. Chan, A.H. Safavi-Naeini, J.T. Hill, S. Meenehan, O. Painter, *Appl. Phys. Lett.* **101**(8), (2012)
11. A.H. Safavi-Naeini, J. Chan, J.T. Hill, S. Groeblacher, H. Miao, Y. Chen, M. Aspelmeyer, O. Painter, *New J. Phys* **15**(3), 035007 (2013)
12. COMSOL Multiphysics 3.5, <http://www.comsol.com/>
13. S.G. Johnson, J.D. Joannopoulos, *Opt. Express* **8**(3), 173 (2001)
14. J.V. Bladel, *Electromagnetic Fields, 2ed* (IEEE Press. Wiley-Interscience, 2007)
15. S. Haroche, J.M. Raimond, *Exploring the Quantum: Atoms, Cavities, and Photons* (Oxford University Press, 2006)
16. C. Kittel, *Introduction to Solid State Physics* (John Wiley, 2005)
17. S. John, *Phys. Rev. Lett.* **58**(23), 2486 (1987)
18. E. Yablonovitch, T. Gmitter, J.P. Harbison, R. Bhat, *Appl. Phys. Lett.* **51**, 2222 (1987)
19. M.S. Kushwaha, P. Halevi, L. Dobrzynski, B. Djafari-Rouhani, *Phys. Rev. Lett.* **71**(13), 2022 (1993)
20. M. Sigalas, E. Economou, *Journal of Sound and Vibration* **158**(2), 377 (1992)
21. J. Joannopoulos, S. Johnson, J. Winn, R. Meade, *Photonic Crystals: Molding the Flow of Light* (Princeton University Press, 2008)
22. B.A. Auld, *Acoustic fields and waves in solids*, vol. 1 (Wiley New York, 1973)
23. D. Marcuse, *Theory of dielectric optical waveguides* (Access Online via Elsevier, 1974)
24. K. Graff, *Wave Motion in Elastic Solids* (Dover Publications, 1975)
25. A. Yariv, P. Yeh, *Optical waves in crystals*, vol. 5 (Wiley New York, 1984)
26. A.N. Cleland, *Foundations of nanomechanics: from solid-state theory to device applications* (Springer, 2003)
27. A. Fallahkhair, K. Li, T. Murphy, *Journal of Lightwave Technology* **26**(11), 1423 (2008)
28. A.N. Cleland, M.L. Roukes, *Nature* **392**, 160 (1998)
29. M.D. Chabot, J. Moreland, L. Gao, S.H. Liou, C. Miller, *Microelectromechanical Systems, Journal of* **14**(5), 1118 (2005)
30. P.H. Kim, C. Doolin, B.D. Hauer, A.J.R. MacDonald, M.R. Freeman, P.E. Barclay, J.P. Davis, *Appl. Phys. Lett.* **102**(5), 053102 (2013)
31. J.S. Foresi, P.R. Villeneuve, J. Ferrera, E.R. Thoen, G. Steinmeyer, S. Fan, J.D. Joannopoulos, L.C. Kimerling, H.I. Smith, E.P. Ippen, *Nature* **390**(6656), 143 (1997)
32. C. Sauvan, P. Lalanne, J.P. Hugonin, *Phys. Rev. B* **71**(16), 165118 (2005)
33. P. Barclay, K. Srinivasan, O. Painter, *Opt. Express* **13**, 801 (2005)
34. L.D. Haret, T. Tanabe, E. Kuramochi, M. Notomi, *Opt. Express* **17**(23), 21108 (2009)
35. K. Schwab, E.A. Henriksen, J.M. Worlock, M.L. Roukes, *Nature* **404**(6781), 974 (2000)
36. M. Eichenfield, J. Chan, R. Camacho, K. Vahala, O. Painter, *Nature* **462**(7269), 78 (2009)
37. M. Eichenfield, J. Chan, A.H. Safavi-Naeini, K.J. Vahala, O. Painter, *Opt. Express* **17**(22), 20078 (2009)
38. A.H. Safavi-Naeini, O. Painter, *Opt. Express* **18**(14), 14926 (2010)
39. T.P.M. Alegre, A. Safavi-Naeini, M. Winger, O. Painter, *Opt. Express* **19**, 5658 (2011)
40. P.L. Yu, K. Cicak, N. Kampel, Y. Tsaturyan, T. Purdy, R. Simmonds, C. Regal, arXiv:1312.0962 (2013)

41. A.H. Safavi-Naeini, J.T. Hill, S. Meenehan, J. Chan, S. Groeblacher, O. Painter, arXiv:1401.1493 (2014)
42. K. Srinivasan, O. Painter, Optics Express **10**(15), 670 (2002)
43. Y. Akahane, T. Asano, B.S. Song, S. Noda, Nature **425**(6961), 944 (2003)
44. B.S. Song, S. Noda, T. Asano, Y. Akahane, Nat Mater **4**(3), 207 (2005)
45. M. Borselli, T.J. Johnson, O. Painter, App. Phys. Lett. **88**, 131114 (2006)
46. J. Chan, Laser cooling of an optomechanical crystal resonator to its quantum ground state of motion. Ph.D. thesis, California Institute of Technology (2012)
47. A.R. Md Zain, N.P. Johnson, M. Sorel, R.M. De La Rue, Opt. Express **16**(16), 12084 (2008)
48. M. Notomi, E. Kuramochi, H. Taniyama, Opt. Express **16**(15), 11095 (2008)
49. J. Chan, M. Eichenfield, R. Camacho, O. Painter, Opt. Express **17**(5), 3802 (2009)
50. P.B. Deotare, M.W. McCutcheon, I.W. Frank, M. Khan, M. Loncar, Appl. Phys. Lett. **94**(12), 121106 (2009)
51. S.G. Johnson, M. Ibanescu, M.A. Skorobogatiy, O. Weisberg, J.D. Joannopoulos, Y. Fink, Phys. Rev. E **65**(6), 066611 (2002)
52. M.J. Burek, N.P. de Leon, B.J. Shields, B.J.M. Hausmann, Y. Chu, Q. Quan, A.S. Zibrov, H. Park, M.D. Lukin, M. Lonar, Nano Lett. **12**(12), 6084 (2012)
53. L. Li, M. Trusheim, O. Gaathon, K. Kisslinger, C.J. Cheng, M. Lu, D. Su, X. Yao, H.C. Huang, I. Bayn, Journal of Vacuum Science & Technology B **31**(6), 06FF01 (2013)
54. P. Rath, S. Khasminskaya, C. Nebel, C. Wild, W.H. Pernice, Nat Commun **4**, 1690 (2013)
55. M. Radulaski, T.M. Babinec, S. Buckley, A. Rundquist, J. Provine, K. Alassaad, G. Ferro, J. Vuckovic, Opt. Express **21**(26), 32623 (2013)
56. J. Cardenas, M. Zhang, C.T. Phare, S.Y. Shah, C.B. Poitras, B. Guha, M. Lipson, Opt. Express **21**(14), 16882 (2013)
57. C.P. Michael, M. Borselli, T.J. Johnson, C. Chrystal, O. Painter, Opt. Express **15**, 4745 (2007)
58. B.D. Hauer, P.H. Kim, C. Doolin, A.J. MacDonald, H. Ramp, J.P. Davis, arXiv:1401.5482 (2014)
59. J. Thompson, T. Tiecke, N. de Leon, J. Feist, A. Akimov, M. Gullans, A. Zibrov, V. Vuleti, M. Lukin, Science **340**(6137), 1202 (2013)
60. A.H. Safavi-Naeini, S. Groblacher, J.T. Hill, J. Chan, M. Aspelmeyer, O. Painter, Nature **500**(7461), 185 (2013)
61. S. Groeblacher, J.T. Hill, A.H. Safavi-Naeini, J. Chan, O. Painter, Appl. Phys. Lett. **103**(18), 181104 (2013)
62. M. Fleischhauer, A. Imamoglu, J.P. Marangos, Rev. Mod. Phys. **77**(2), 633 (2005)
63. S. Weis, R. Rivière, S. Deléglise, E. Gavartin, O. Arcizet, A. Schliesser, T.J. Kippenberg, Science **330**, 1520 (2010)
64. E. Gavartin, R. Braive, I. Sagnes, O. Arcizet, A. Beveratos, T.J. Kippenberg, I. Robert-Philip, Phys. Rev. Lett. **106**(20), 203902 (2011)
65. J. Gomis-Bresco, D. Navarro-Urrios, M. Oudich, S. El-Jallal, A. Griol, D. Puerto, E. Chavez, Y. Pennec, D. Djafari-Rouhani, F. Alzina, A. Martnez, C.M. Sotomayor Torres, arXiv:1401.1691 (2014)
66. S.J.M. Habraken, K. Stannigel, M.D. Lukin, P. Zoller, P. Rabl, New Journal of Physics **14**(11), 115004 (2012)
67. A. Tomadin, S. Diehl, M.D. Lukin, P. Rabl, P. Zoller, Phys. Rev. A **86**(3), 033821 (2012)
68. M. Ludwig, F. Marquardt, Phys. Rev. Lett. **111**, 073603 (2013)
69. P. Rabl, Phys. Rev. Lett. **107**(6), 63601 (2011)
70. A. Nunnenkamp, K. Borkje, S. Girvin, Phys. Rev. Lett. **107**(6), 63602 (2011)
71. M. Ludwig, A.H. Safavi-Naeini, O. Painter, F. Marquardt, Phys. Rev. Lett. **109**(6), 063601 (2012)
72. K. Stannigel, P. Komar, S.J.M. Habraken, S.D. Bennett, M.D. Lukin, P. Zoller, P. Rabl, Phys. Rev. Lett. **109**, 013603 (2012)
73. M. Davanco, J. Chan, A.H. Safavi-Naeini, O. Painter, K. Srinivasan, Optics Express **20**(22), 24394 (2012)
74. H. Sekoguchi, Y. Takahashi, T. Asano, S. Noda, Optics Express **22**(1), 916 (2014)
75. J. Bochmann, A. Vainsencher, D.D. Awschalom, A.N. Cleland, Nature Physics (2013)